JGR Planets

RESEARCH ARTICLE
10.1029/2019JE006322

Special Section:
Investigations of Vera Rubin Ridge, Gale Crater

Diagenesis of Vera Rubin Ridge, Gale Crater, Mars, From Mastcam Multispectral Images

Briony H. N. Horgan[1], Jeffrey R. Johnson[2], Abigail A. Fraeman[3], Melissa S. Rice[4], Christina Seeger[4,9], James F. Bell III[5], Kristen A. Bennett[6], Edward A. Cloutis[7], Lauren A. Edgar[6], Jens Frydenvang[8], John P. Grotzinger[9], Jonas L'Haridon[10], Samantha R. Jacob[5], Nicolas Mangold[10], Elizabeth B. Rampe[11], Frances Rivera-Hernandez[12], Vivian Z. Sun[3], Lucy M. Thompson[13], and Danika Wellington[5]

[1]Department of Earth, Atmospheric, and Planetary Sciences, Purdue University, West Lafayette, IN, USA, [2]Johns Hopkins University Applied Physics Laboratory, Laurel, MD, USA, [3]Jet Propulsion Laboratory, California Institute of Technology, Pasadena, CA, USA, [4]Geology Department, Physics and Astronomy Department, Western Washington University, Bellingham, WA, USA, [5]School of Earth and Space Exploration, Arizona State University, Tempe, AZ, USA, [6]U.S. Geological Survey, Astrogeology Science Center, Flagstaff, AZ, [7]Department of Geography, University of Winnipeg, Winnipeg, Manitoba, Canada, [8]Globe Institute, University of Copenhagen, Copenhagen, Denmark, [9]Division of Geological and Planetary Sciences, California Institute of Technology, Pasadena, CA, USA, [10]Laboratoire de Planétologie et Géodynamique, CNRS, Univ Nantes, Univ Angers, Nantes, France, [11]NASA Johnson Space Center, Houston, TX, USA, [12]Department of Earth Sciences, Dartmouth College, Hanover, NH, USA, [13]Planetary and Space Science Centre, University of New Brunswick, Fredericton, New Brunswick, Canada

Key Points:
- Vera Rubin ridge exhibits strong color differences that crosscut stratigraphy, consistent with postdepositional alteration (diagenesis)
- Color differences correspond to variations in spectral signatures of nanophase, fine-grained, and coarse-grained hematite
- Based on terrestrial analogs, these variations can be explained by early oxidation and later coarsening of hematite by diagenetic fluids

Supporting Information:
- Supporting Information S1
- Table S2

Correspondence to:
B. H. N. Horgan,
briony@purdue.edu

Citation:
Horgan, B. H. N., Johnson, J. R., Fraeman, A. A., Rice, M. S., Seeger, C., Bell, J. F., III, et al. (2020). Diagenesis of Vera Rubin ridge, Gale crater, Mars, from Mastcam multispectral images. *Journal of Geophysical Research: Planets*, *125*, e2019JE006322. https://doi.org/10.1029/2019JE006322

Received 10 DEC 2019
Accepted 19 SEP 2020
Accepted article online 23 SEP 2020

Abstract Images from the Mars Science Laboratory (MSL) mission of lacustrine sedimentary rocks of Vera Rubin ridge on "Mt. Sharp" in Gale crater, Mars, have shown stark color variations from red to purple to gray. These color differences crosscut stratigraphy and are likely due to diagenetic alteration of the sediments after deposition. However, the chemistry and timing of these fluid interactions is unclear. Determining how diagenetic processes may have modified chemical and mineralogical signatures of ancient Martian environments is critical for understanding the past habitability of Mars and achieving the goals of the MSL mission. Here we use visible/near-infrared spectra from Mastcam and ChemCam to determine the mineralogical origins of color variations in the ridge. Color variations are consistent with changes in spectral properties related to the crystallinity, grain size, and texture of hematite. Coarse-grained gray hematite spectrally dominates in the gray patches and is present in the purple areas, while nanophase and fine-grained red crystalline hematite are present and spectrally dominate in the red and purple areas. We hypothesize that these differences were caused by grain-size coarsening of hematite by diagenetic fluids, as observed in terrestrial analogs. In this model, early primary reddening by oxidizing fluids near the surface was followed during or after burial by bleaching to form the gray patches, possibly with limited secondary reddening after exhumation. Diagenetic alteration may have diminished the preservation of biosignatures and changed the composition of the sediments, making it more difficult to interpret how conditions evolved in the paleolake over time.

Plain Language Summary Sedimentary rocks found in deserts on Earth often exhibit striking color differences from red and purple to white, which are caused by groundwater dissolving and reprecipitating iron oxides within the rocks. NASA's Mars Science Laboratory (MSL) mission has observed similar color differences on Mars within the sedimentary rocks of Vera Rubin ridge in Gale crater, which were laid down in an ancient lake. We use color images and spectral data from the Mastcam cameras on MSL to investigate the origin of these color differences and find that they are consistent with changes in iron oxides through the ridge. This variation in iron oxides suggests that groundwater flowed through and altered these rocks multiple times before and after they were buried by later sediments. The MSL mission has shown that habitable lake environments once existed in Gale crater, through detections of the building blocks of life, including organic molecules, and by showing that conditions that existed in the lake were clement for life. However, later alteration by groundwater may have diminished the preservation of organics and changed the composition of these rocks, making it more difficult to interpret the details of how conditions evolved in the lake over time.

1. Introduction

One of the major recent paradigm shifts in planetary geology has been the recognition that the surface of Mars, although home to some of the largest volcanoes in the solar system, is dominated by stratified sedimentary rocks (e.g., Edgett, 2016; Grotzinger & Milliken, 2012; Malin & Edgett, 2000, 2001; McLennan et al., 2018). These layers provide a long-term record of the history of climate, environment, and life on Mars, but interpreting this record requires understanding sediment sources, sediment transport histories, alteration, and mechanisms for lithification of these globally widespread deposits (e.g., Grotzinger et al., 2011). The chemical and physical changes that occur during the process of turning sediment into sedimentary rock (through cementation, burial, compaction, and subsurface alteration) are collectively referred to as diagenesis. On Mars, determining the fluid chemistries, temperatures, timescales, and frequency of diagenetic events is particularly critical for constraining how these processes may have affected the long-term preservation of organics and biosignatures in the rock record (Hays et al., 2017; Summons et al., 2011).

However, our knowledge of diagenetic fluid properties on Mars is limited, as identifying unique signatures of diagenetic processes in orbital observations is challenging. Our deepest understanding of diagenesis on Mars to date has come from in situ rover investigations of sedimentary rocks in a few locations across the planet (McLennan et al., 2018). Both the Mars Science Laboratory (MSL/Curiosity; Grotzinger et al., 2012) and the Mars Exploration Rover (MER-A/Spirit and MER-B/Opportunity; Crisp et al., 2003) missions have found physical and chemical evidence for early and late diagenetic processes on Mars. This includes carbonate, silica, and sulfate cements (e.g., Grotzinger et al., 2014; Rapin et al., 2019; Ruff et al., 2011, 2014; Siebach et al., 2014), diagenetic concretions, nodules, crystal molds/vugs, and secondary porosity (Grotzinger et al., 2005; McLennan et al., 2005; Stack et al., 2014; Nachon et al., 2017, Sun et al., 2018), filled fractures (Kronyak et al., 2019; L'Haridon et al., 2018; Nachon et al., 2014, 2016; Rapin et al., 2016), and halo-bounded fractures (Frydenvang et al., 2017; Yen et al., 2017). Collectively, these diagenetic features suggest a complex history of fluid interactions before, during, and after sediment deposition on Mars.

In this study, we investigate a new category of possible diagenetic features on Mars: large-scale color variations within bedrock. In 2017, Curiosity climbed onto Vera Rubin ridge (VRR; Figure 1), a topographic ridge on the lower northwest flank of Aeolis Mons (informally known as Mt. Sharp) with strong hematite signatures in orbital visible/near-infrared (IR) spectra (Fraeman et al., 2013). Among the red rocks of VRR, Curiosity encountered a series of decameter-scale light-toned gray to blue patches (Figure 2). The color contrast crosscuts sedimentary layers and is not accompanied by any clear change in physical or sedimentological properties (Edgar et al., 2020). Similar color variability is often observed in sedimentary sequences on Earth and is typically due to alteration during or after burial by chemically distinct diagenetic fluids (e.g., Bowen et al., 2007). On Earth, these exposed diagenetic patterns are used to help understand subsurface fluid sources, chemistries, residence times, and flow paths (e.g., Eichhubl et al., 2004), and comparison to these examples may provide constraints on the aqueous history of Gale crater sediments (e.g., Chan et al., 2005).

Here we use visible/near-IR (447–1,013 nm) color images and multispectral data from the Mastcam imaging system on MSL (Bell et al., 2017; Malin et al., 2017), supported by spectral and compositional data from other rover instruments, to investigate the nature and timing of fluid interactions on VRR. We seek to constrain the mineralogical variations responsible for spectral and color variations across VRR and to evaluate the relationship between the gray patches and other VRR color units. By comparing our derived mineralogies to terrestrial analogs, we investigate which diagenetic processes (early vs. late; fluid chemistry vs. temperature; e.g., Montañez & Crossey, 2018) could have caused the observed color variations. Unraveling which physical and compositional rock properties in Gale are the result of environmental conditions during deposition versus later diagenesis is critical for determining the nature and habitability of early Martian surface environments and fulfilling the MSL mission goals.

2. Background

Curiosity landed in Gale crater in 2012 with the goal of exploring the ancient habitability of Mars (Grotzinger et al., 2012). Gale is a 154 km diameter crater that contains a massive 5 km high central mound of layered

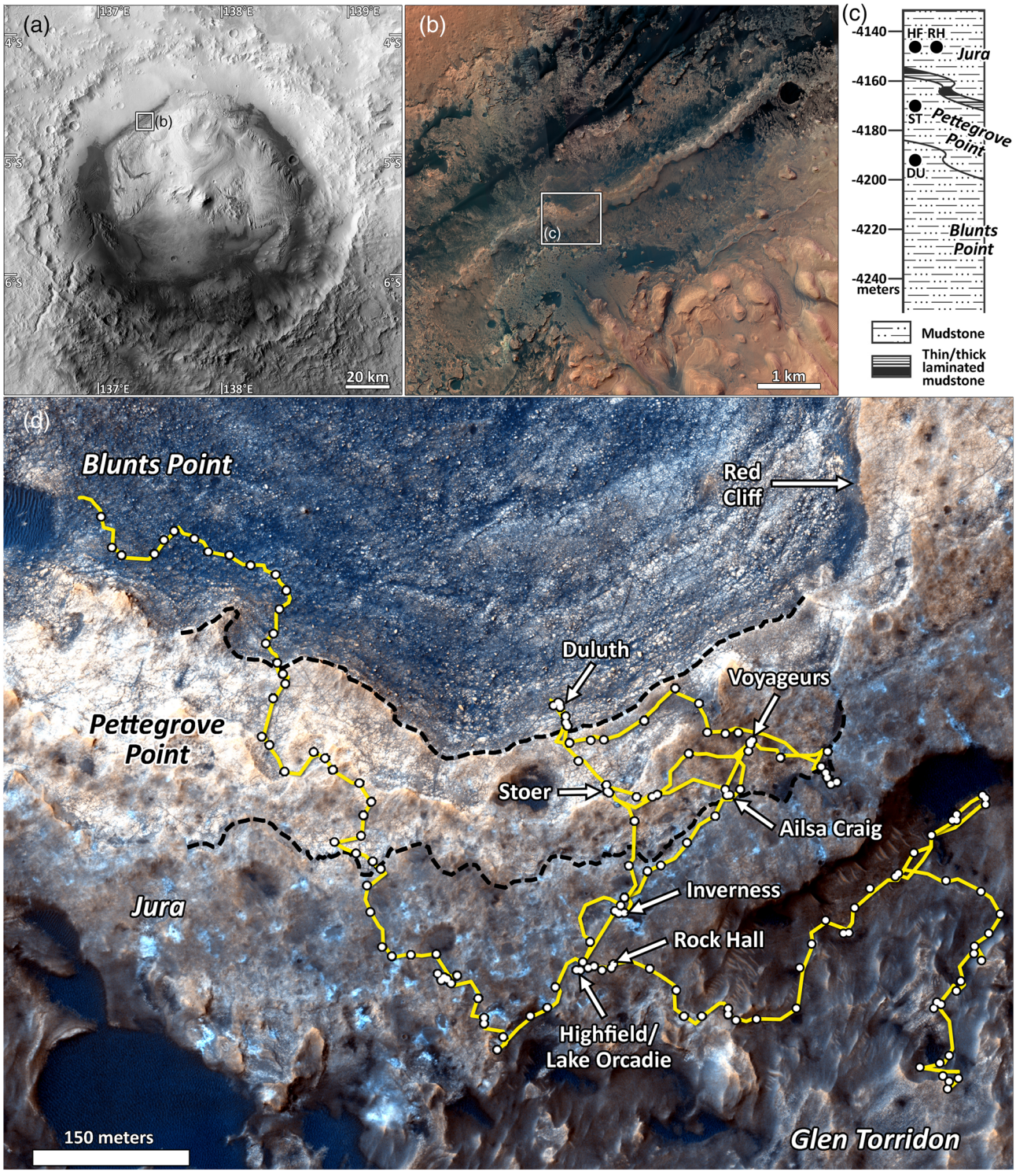

Figure 1. Overview of Vera Rubin ridge (VRR) from orbital images, taken with illumination from left. (a) CTX mosaic of Gale crater. (b) HiRISE approximate true-color mosaic over Murray formation. (c) Section of the stratigraphic column for the Murray formation corresponding to VRR, where sinuous lines indicate variable contact elevations, and successful drill locations (dots) are labeled with acronyms used in text (Edgar et al., 2020). (d) HiRISE enhanced-color RGB image ESP_042682_1755 showing the region of VRR explored by MSL, enhanced to emphasize variability. Black dashed lines indicate inferred member boundaries (Edgar et al., 2020), yellow line indicates drive path of Curiosity, and white points indicate stops by Curiosity. Labels indicate all attempted drill sites and Red Cliff (Figure 15).

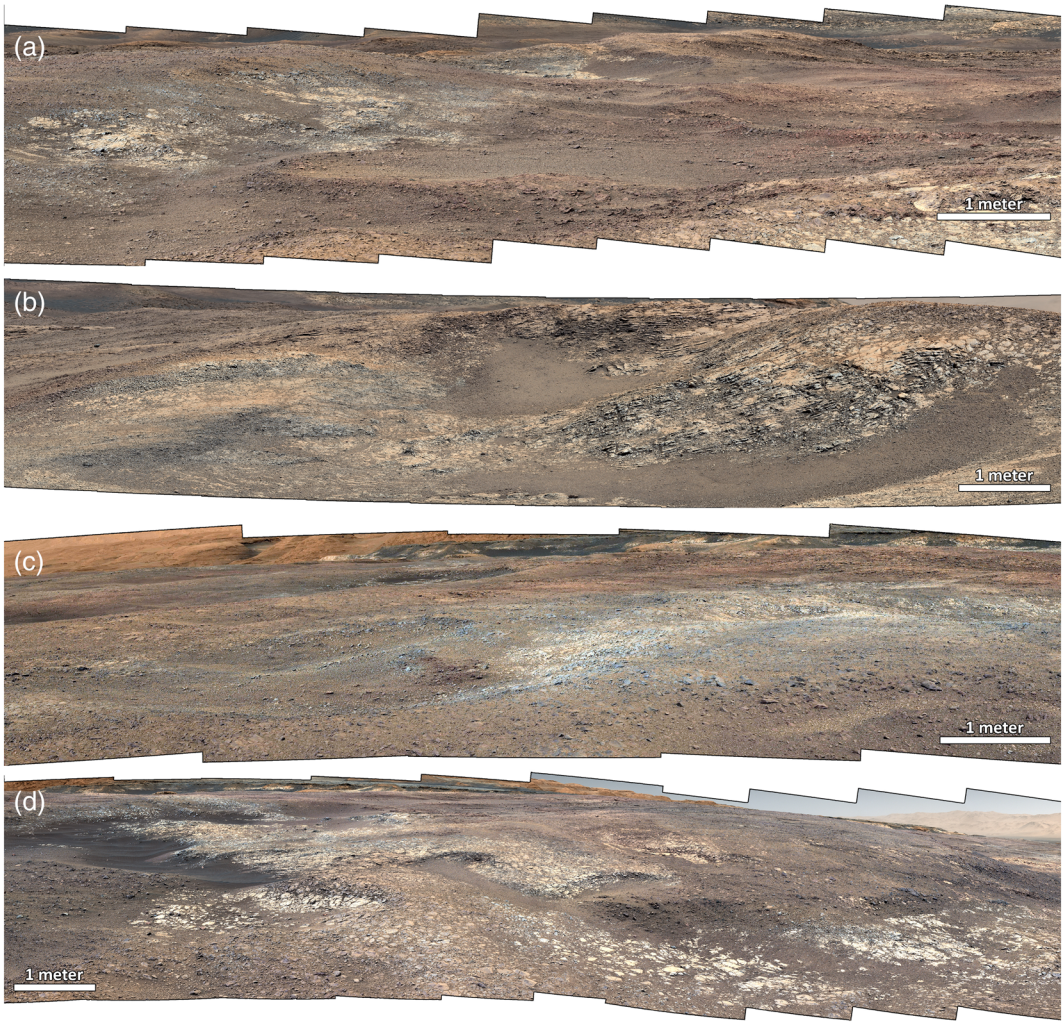

Figure 2. Examples of color differences in the Jura member of VRR, as observed by Mastcam in white-balanced and enhanced RGB Bayer filters. (a) R0 mosaic mcam10002 on Sol 1,906, (b) R0 mosaic mcam10158 on Sol 1,942, (c) L0 mosaic mcam09885 on Sol 1,889, and (d) L0 mosaic mcam10419 on Sol 1,988. White bars indicate approximate scale in foreground for reference. Viewsheds for these mosaics on orbital images are shown in Figure S1.

sedimentary rock known as Mt. Sharp (Anderson & Bell, 2010; Malin & Edgett, 2000; Thomson et al., 2011). In situ results from over 20 km of traverse to date by Curiosity have shown that Mt. Sharp records a series of ancient surface environments that contained the building blocks of life under conditions clement for life on Earth and were thus interpreted as habitable (Grotzinger et al., 2014). Much of the base of Mt. Sharp is composed of the Murray formation, a sequence of fine-grained mudstones, siltstones, and sandstones that were deposited in a long-lived fluviolacustrine environment (Edgar et al., 2020; Grotzinger et al., 2015; Rivera-Hernández et al., 2020). The total thickness of the Murray formation to date exceeds 300 m, and the top of the formation has not yet been identified (Fedo et al., 2018).

Orbital investigations of Mt. Sharp have shown clear spectral signatures of secondary minerals due to aqueous alteration, including hematite, phyllosilicates, and sulfates (Fraeman et al., 2013, 2016; Milliken et al., 2010, 2014). Spatial variations in these signatures were hypothesized to reflect different surface environments related to changing climates on Mars from the Noachian into the Hesperian eras, and thus, these strata could provide a detailed record of surface habitability on Mars through time (Milliken et al., 2010). X-ray diffraction analysis of drill samples by the MSL CheMin instrument (Blake et al., 2012) has confirmed that the mineral assemblage of bedrock in the Murray formation includes variable abundances of phyllosilicates, sulfates, and iron oxides (Rampe et al., 2017). However, whether these alteration minerals formed in

a lacustrine environment or through later diagenetic processes remains uncertain. While the phyllosilicates are variably consistent with either detrital deposition or authigenic formation in a lake (Bristow et al., 2018), both lacustrine and diagenetic origins have been postulated for the iron oxides (Hurowitz et al., 2017; Rampe et al., 2017) and sulfates (Rampe et al., 2017; Rapin et al., 2019). In addition, iron oxide concretions (Sun et al., 2018), sulfate-filled concretions and fractures (Kronyak et al., 2019; L'Haridon et al., 2018; Nachon et al., 2017), and halo-bounded silica-rich fractures (Frydenvang et al., 2017; Yen et al., 2017) throughout the Murray provide clear evidence for diagenesis after lithification, likely through multiple alteration events with variable fluid chemistries.

VRR is a topographic feature ~6.5 km long and ~200 m wide on the northwestern flank of Mt. Sharp (Anderson & Bell, 2010; Fraeman et al., 2013). The base of the taller north-facing (downhill) cliff of VRR corresponds to the Blunts Point member, a fine-grained recessive facies with extensive planar lamination and abundant calcium sulfate veins (Edgar et al., 2020; Fedo et al., 2019). Stratigraphically above the Blunts Point member, steep cliffs at the top of the north side of the ridge correspond to the Pettegrove Point member. While the Pettegrove Point member is physically similar to the Blunts Point member, it is more erosionally resistant and exhibits fewer sulfate veins and more diagenetic features (Bennett et al., 2020; Edgar et al., 2020; Tinker et al., 2019). The Pettegrove Point member is overlain by the Jura member and together form the top of the ridge. The Jura member is still finely laminated but also exhibits much more variability in color, texture, and sedimentary structures compared to the Pettegrove Point or Blunts Point members (Bennett et al., 2020). The contact between the Pettegrove Point and Jura members occurs along with a distinct step in topography, corresponding to large-scale inclined beds and a distinct facies defined by alternating thinly and thickly laminated packages of mudstone to fine sandstone, known as the "Flodigarry" facies (Edgar et al., 2020). Gray patches on VRR are dominantly found within the Jura member but also occur sporadically within the Pettegrove Point member (Figure 1). The Jura member exhibits abundant dark diagenetic features, most commonly dark nodules and crystal forms interpreted as iron oxide-filled crystal molds after gypsum pseudomorphs but also partial vein fills and euhedral crystals in light-toned veins (Bennett et al., 2020; L'Haridon et al., 2020; Tinker et al., 2019). The shorter south-facing (uphill) cliff of VRR runs down into the phyllosilicate-bearing Glen Torridon unit (Fox et al., 2019).

Three drilled samples were successfully collected on VRR as well as one below, one each in the Blunts Point (Duluth [DU]) and Pettegrove Point (Stoer [ST]) members and two targets in the Jura member (Highfield [HF] and Rock Hall [RH]). Four other drill attempts were made across the Pettegrove Point and Jura members but did not complete due to rock hardness beyond the capabilities of the percussive drill on MSL (see Fraeman, Edgar, et al., 2020, for complete details of the VRR campaign). All drill targets are labeled in Figure 1d. CheMin analyses of the successfully drilled samples showed a variety of secondary minerals relevant to the spectral analyses in this study (Rampe et al., 2020), including crystalline hematite (DU: 6.1%, ST: 15%, HF: 8.5%, and RH: 2.9%, where abundances are reported as wt.% of the bulk sample), magnetite (DU: 1.7%, ST: 0.3%, and HF: 0.5%; values near detection limit of CheMin), akaganeite (ST: 1.2% and RH: 6.0%), jarosite (ST: 1.0% and RH: 2.3%), phyllosilicates (DU: 15%, ST: 10%, HF: 5%, and RH: 13%), opal CT (HF: 4%), and amorphous materials (DU: 37%, ST: 38%, HF: 49%, and RH: 34%).

3. Methods

3.1. Orbital Images

Images from the Mars Reconnaissance Orbiter (MRO) High Resolution Imaging Science Experiment (HiRISE) camera (McEwen et al., 2007) have a sufficiently small pixel scale (~26.5 cm/pixel at the latitude of Gale crater) to enable detection of color variations on VRR. Here we use an enhanced-color composite from HiRISE observation ESP_042682_1755 (Figure 1) made from HiRISE's three-color filters: blue-green (BG: 502 ± 157 nm), red (RED: 686 ± 267 nm), and near IR (878 ± 143 nm), with BG and IR data are available only for a central strip covering 20% of each RED image. HiRISE color data presented here are used only to assess qualitative color variations.

3.2. Mastcam

The Mast Camera imaging system, or Mastcam, is a pair of cameras located ~2 m above the surface, mounted on the rover's remote sensing mast, and utilizes filter wheels to provide high-resolution visible/near-IR (445–1,013 nm) multispectral imaging of the terrain around Curiosity (Bell et al., 2017; Malin et al., 2017).

The cameras operate at two different fixed focal lengths, with the right camera (M100) providing higher resolution images at 100 mm focal length and the left camera (M34) providing context imaging at 34 mm focal length. Both cameras make use of 1,600 × 1,200 CCDs with a Bayer pattern filter set bonded to the detectors. The filter wheels each hold six narrowband VNIR filters, one narrowband neutral density filter for solar observations, and a broadband IR-cutoff filter for Bayer color imaging. Filters with band passes centered at ~445, ~527, and ~1,013 nm are included on both cameras, with the other filters distributed between the cameras (Bell et al., 2017; supporting information Table S1). The absolute radiometric accuracy for Mastcam is <±10%, with a filter-to-filter precision of <±7% (Bell et al., 2017).

Raw Mastcam images are calibrated to radiance ($W/m^2/nm/sr$) using preflight calibration measurements, as described in Bell et al. (2017). Radiance images are then converted to radiance factor (I/F), or the ratio of the measured scene radiance (I) to the solar irradiance at Mars (πF), using recent, similar-time observations of the Mastcam radiometric calibration target on the rover deck, corrected for illumination and viewing geometry, atmospheric scattering, and dust deposition (Bell et al., 2017; Kinch et al., 2015; Wellington et al., 2017). Radiance factor images are then converted to relative reflectance (R^*) by dividing by the cosine of the solar incidence angle at the time of imaging. Calibrated Mastcam images can be "white balanced" by linearly scaling them with a set of coefficients developed from preflight testing (e.g., Figure 2; Bell et al., 2017). The white-balanced stretches approximate color under Earth-like illumination conditions.

Mastcam's three Bayer filters and additional narrowband filters allow multispectral imaging in 12 unique wavelengths between 445 and 1,013 nm. Spectra extracted from these images can be used together to identify a variety of mineral groups and sometimes specific mineral phases (e.g., Johnson et al., 2017; Wellington et al., 2017). Within this range, the most dominant absorption bands are typically due to iron, including bands from crystal field effects in Fe-bearing silicates like olivine and pyroxene between 900 and 1,300 nm (Adams, 1968; Cloutis & Gaffey, 1991; Horgan et al., 2014); spin-forbidden transitions in Fe^{3+}-bearing oxides like hematite and goethite near 800–1,000 nm (Morris et al., 1985; Townsend, 1987); and charge transfer between Fe^{2+} and Fe^{3+} in iron oxides and hydroxides between 400 and 500 nm (Morris et al., 1985; Sherman, 1990). Mastcam is also sensitive to some hydrated minerals due to a weak H_2O overtone absorption near 980 nm (Rice et al., 2010, 2013). Figure 3 shows example hyperspectral VNIR/SWIR lab spectra of Fe-bearing minerals convolved with the 12 Mastcam Bayer and narrowband filter band passes (Bell et al., 2017), illustrating that Mastcam multispectral spectra are generally able to differentiate the majority of these phases based on the position and shape of the various Fe absorption bands.

In this study, we examined Mastcam full-filter ("Lall/Rall") multispectral images acquired between Sols 1,809 and 2,300 (see Table S2), calibrated and processed to relative reflectance. In total, this sol range included 113 Lall/Rall science imaging sequences. This study specifically focuses on images corresponding to all drill sites and attempted drill sites, all workspace mosaics (images of the ground within the rover's arm reachability), landscape mosaics showing major bedrock color transitions, and a color-representative subset of the images that include targets cleared by the dust removal tool (DRT). Targets analyzed in this study are listed in Table S3 by stratigraphic member and color unit, and the locations of all attempted and successful drill sites are shown in Figure 1d. Observation parameters for images used to generate spectral plots are shown in Table S2. Landscape color (non-multispectral) image mosaics across the traverse also help to provide context for multispectral data and to understand the broader relationship between color units.

Colors and short-wavelength spectral contrast are negatively affected by moderate to high atmospheric opacity due to increased dust in the atmosphere, which is most pronounced during dust storms. A major dust storm rapidly began on Sol 2,075, peaked between Sols 2,086 and 2,090, and gradually decreased to near pre-storm levels by about Sol ~2,140 (Smith et al., 2019). In this study, we have avoided images taken during these higher opacity periods where possible. High opacities correspond to elevated optical depth (tau) values, as reported in Table S2 (Guzewich et al., 2019; Lemmon et al., 2019). Notable exceptions include the Voyageurs drill site (Sols 2,110 and 2,113; Figures 5 and 11), which exhibits such strong spectral contrast that it is not significantly affected by the slightly elevated opacities at that time.

Each M100 (Rall) image within a mosaic was assessed individually along with its corresponding M34 (Lall) image. Color and spectral diversity was qualitatively evaluated in each image using white-balanced approximate true-color images (Figure 2), enhanced-color stretches applied to Bayer filter images ("R0/L0"; Figure 7a), enhanced-color RGB combinations including longer wavelength filters (e.g., R312/L512 to

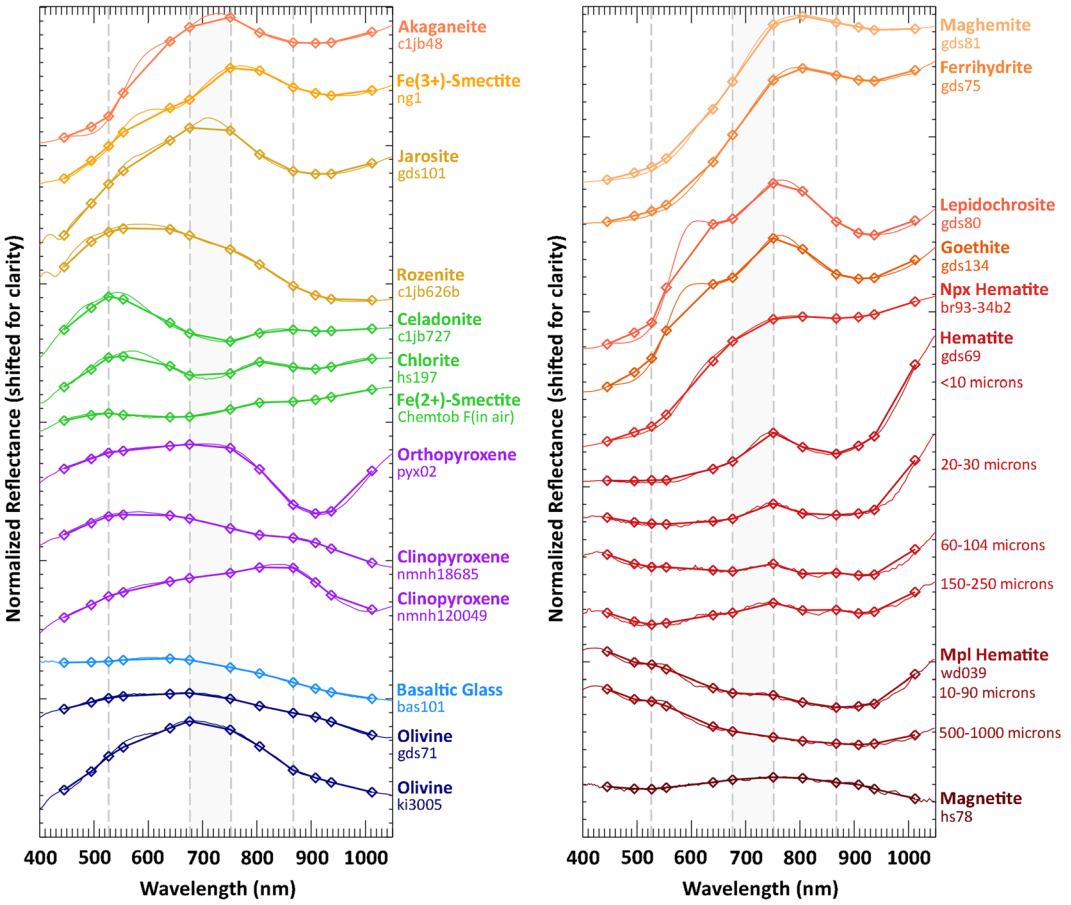

Figure 3. Laboratory spectra of (left) common primary and secondary Fe-bearing minerals and (right) iron oxides. Hematite spectral variations with grain size and texture are also shown, including nanophase (Npx) and microplaty (Mpl) hematite (Lane et al., 2002; Morris et al., 1989). Thin lines are original laboratory spectra, and thick lines and points are these spectra convolved with Mastcam spectral band passes (Bell et al., 2017). To more clearly emphasize spectral properties, all spectra have been normalized to their maximum value in this wavelength range. Vertical dashed lines indicate the locations of common absorptions in VRR, and the gray box indicates the general location of a wide shoulder observed near ~700 nm.

highlight differences in iron oxide charge transfer absorptions; Figures 10–14), and decorrelation stretches applied to various band combinations (Gillespie et al., 1986; Figure 7b). Jura color units (i.e., "red" vs. "mottled" vs. "gray") were visually assigned based on texture and color properties in these images as discussed in sections 4.2 and 4.3.

Regions of interest (ROIs) were identified within each M100 (right) image to sample the range of spectral diversity within bedrock, cobbles, DRT spots, and drill tailings. An average spectrum and standard deviations for each band were extracted from each ROI. Spectra were then extracted from approximately corresponding ROIs within the overlapping M34 (left) image. The M34 and M100 spectra were then combined, where small differences in reflectance between the M34 and M100 were accounted for by scaling the M100 spectrum to the M34 spectrum at the longest wavelength (1,013 nm), which is least affected by dust and thus the dust correction. Other overlapping channels are averaged. The minimum ROI size is primarily limited by the resolution of the M34, which has one third the resolution of the M100. The smallest ROI here contains at least ~6 pixels in the M34 image, but typical ROIs are larger. The maximum ROI size is limited by the local bedrock heterogeneity, assessed based on the enhanced-color and DCS images, typically on the order of <20 pixels in the M34. Spectral parameters were calculated for all collected spectra as shown in Figure 8, including band depth (% difference below the continuum; Clark & Roush, 1984) at ~860 nm (center at 867 nm and shoulders at 805 and 908 nm), band depth at ~700 nm (center at 676 nm and shoulders at 639 and 805 nm), and red/blue ratio (approximated by a ratio of 639/527 nm).

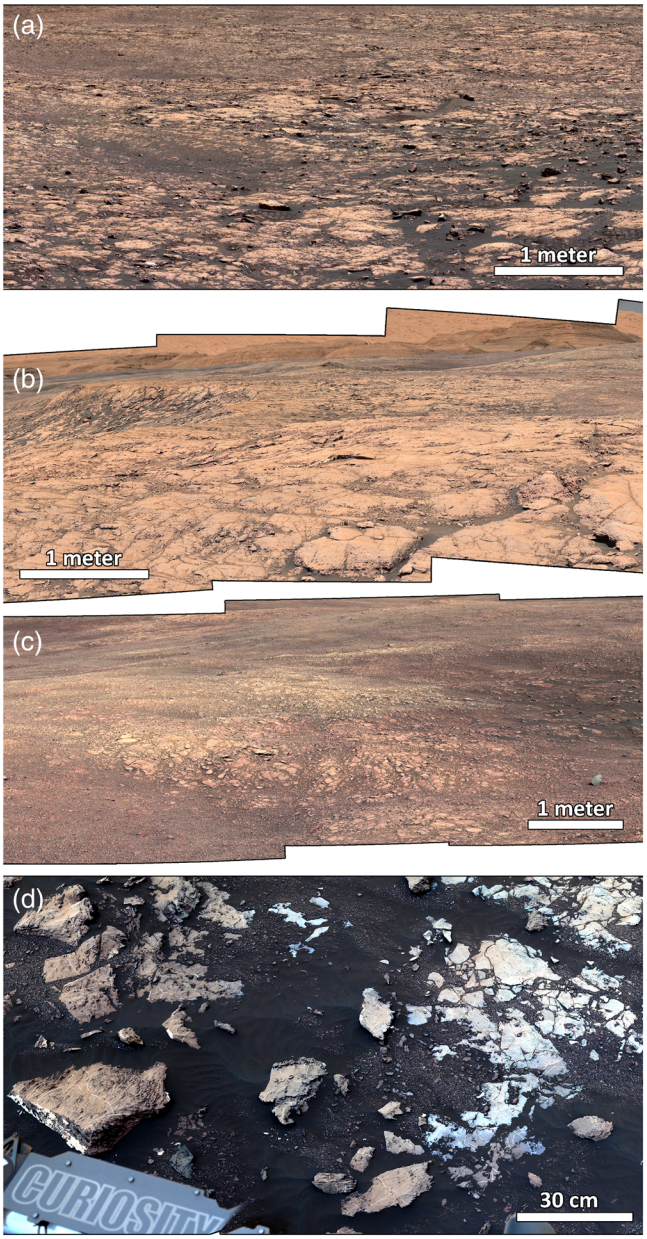

Figure 4. Comparison of red-toned landscapes in the Pettegrove Point and Jura members as observed by Mastcam in RGB Bayer filters, white balanced unless otherwise noted. (a) Pettegrove Point L0 mosaic mcam10608 on Sol 2,013 and (b) Pettegrove Point L0 mosaic mcam09471 on Sol 1,830, showing smooth texture. (c) Jura L0 mosaic mcam12082 on Sol 2,256 in the vicinity of Rock Hall showing rubbly texture. (d) Example of a small gray patch in Pettegrove Point, in the vicinity of the Stoer drill site, L0 mosaic mcam11410 on Sol 2,129, stretched to enhance color differences (and to compensate for the effects of moderate opacity increase during the 2018 dust storm). White bars indicate approximate scale in foreground for reference. Viewsheds for mosaics (a–c) are shown in Figure S1.

3.3. ChemCam

Mastcam multispectral imaging is complemented by Chemistry and Camera (ChemCam) passive point spectroscopy (400–840 nm), as demonstrated by Johnson et al. (2015, 2016). The primary purpose of ChemCam is to derive elemental chemistry from laser-induced breakdown spectroscopy (LIBS; Maurice et al., 2012; Wiens et al., 2012, 2013); however, the "violet" (382–469 nm) and visible/near-IR (474–906 nm) spectrometers used to detect narrow plasma emission lines can also collect "passive" surface spectra either as part of LIBS calibration or as dedicated measurements (Johnson et al., 2015, 2016). ChemCam passive spectra have a much higher spectral resolution compared to Mastcam (<1 vs. ~14–180 nm, respectively), allowing detailed analysis of the position and depth of absorption bands in the VNIR range. ChemCam in passive spectrum acquisition mode has a 0.65 mrad field of view corresponding to a ~2 mm spot size when observing at 3 m (Wiens et al., 2012), which is somewhat larger than the Mastcam angular instantaneous field of view of 0.074 and 0.220 mrad/pixel for the right and left cameras, respectively (Bell et al., 2017). Thus, our Mastcam ROIs are similar in size to single-point spectra from ChemCam.

Here we have utilized longer exposure passive measurements (30 ms) explicitly collected for spectral interpretation, which increases the signal-to-noise ratio compared to standard 3 ms "dark" exposures used during LIBS observations. Raw data were converted to radiance as described by Johnson et al. (2015). Relative reflectance was derived by multiplying the ratio of the measured radiance to that of the white ChemCam calibration target holder radiance by the known reflectance of the calibration target material (Wiens et al., 2012). The absolute calibration uncertainty for the radiance is estimated as 6–8% (Johnson et al., 2015). The location of the passive spectra measurements was determined by comparison to ChemCam Remote Micro-Imager (RMI) images (Maurice et al., 2012; Wiens et al., 2012).

Analysis of ChemCam passive spectra in this study is limited to targets with overlapping Mastcam full-filter multispectral observations for comparison purposes only (listed in Table S2), but additional ChemCam analyses for VRR are presented elsewhere in this issue (Fraeman, Johnson, et al., 2020; Jacob et al., 2020; L'Haridon et al., 2020). Because short wavelengths are strongly affected by high opacities during the dust storm, here we only use ChemCam passive spectra outside of the main dust storm period. All ChemCam spectra are shown in Figure 9. Spectral parameters were calculated for ChemCam by averaging reflectance values within 5 nm of wavelengths of interest. These parameters included red/blue ratio (approximated by a ratio of 639/527 nm) and VNIR slope (ratio of 840/750 nm). ChemCam spectral parameters are plotted in Figure S2.

4. Color Units on VRR

4.1. Large-Scale Color Differences

Color variations on VRR are apparent even at orbital scales, as shown in the HiRISE image in Figure 1. In this enhanced-color stretch, the Pettegrove Point member appears brighter and redder than the Jura member, which shows a darker, more purple color. VRR also shows bright blue patches in this enhanced-color stretch, which correspond to gray patches in true color images. The gray patches are distributed throughout the Jura member and occur along the full extent of VRR. Indeed, the

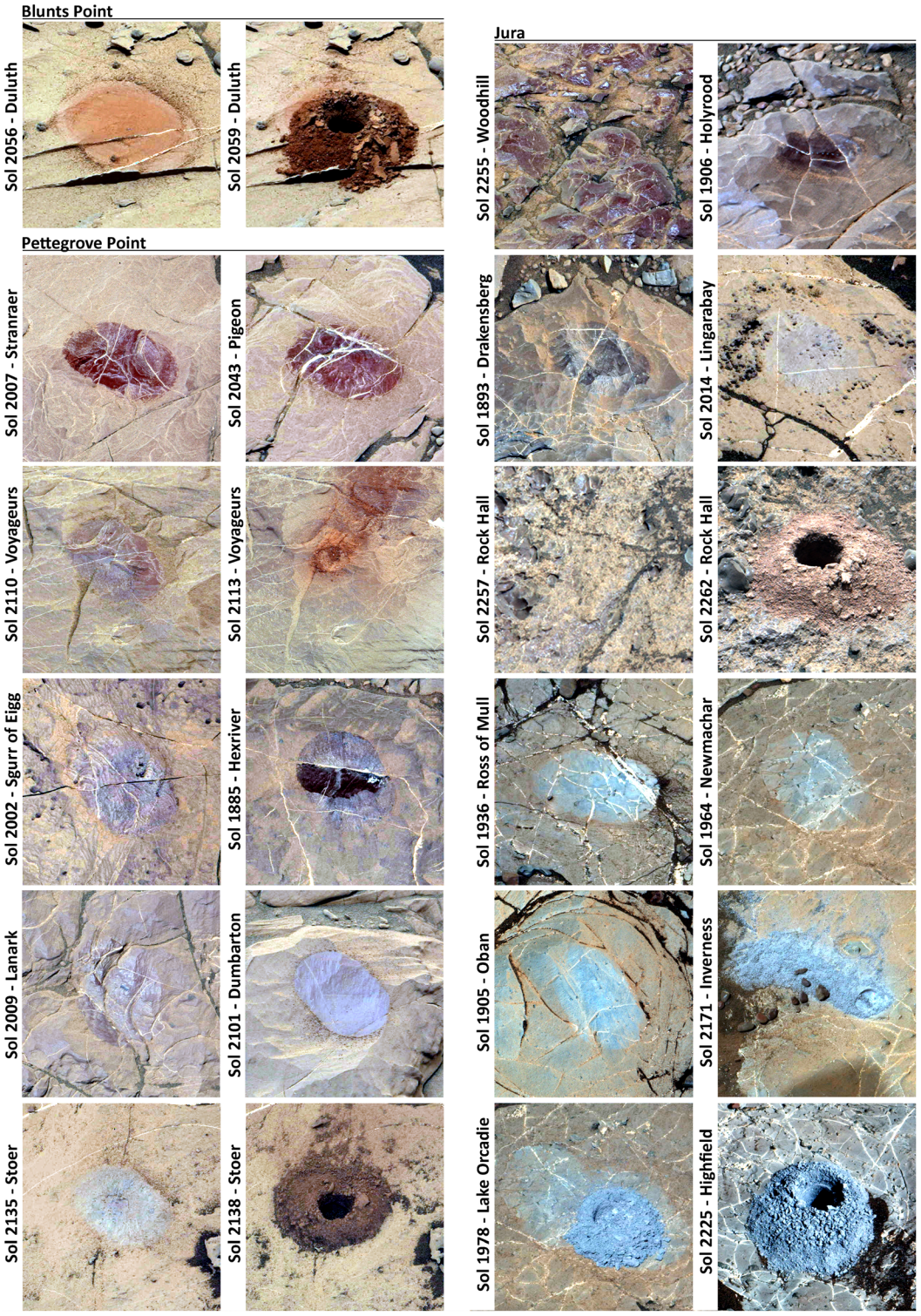

Figure 5. DRT spots, drill tailings, and other relatively dust-free bedrock targets on VRR as observed by Mastcam in R0 Bayer color filters, stretched to enhance color contrast and to maintain similar colors across all dusty bedrock surfaces. Where available, pairs of images show bedrock prior to drilling on left and drill tailings on right. A subset of these targets is shown in R312 filters in Figures 10–14. DRT spots are typically ~7.5 × 4.5 cm.

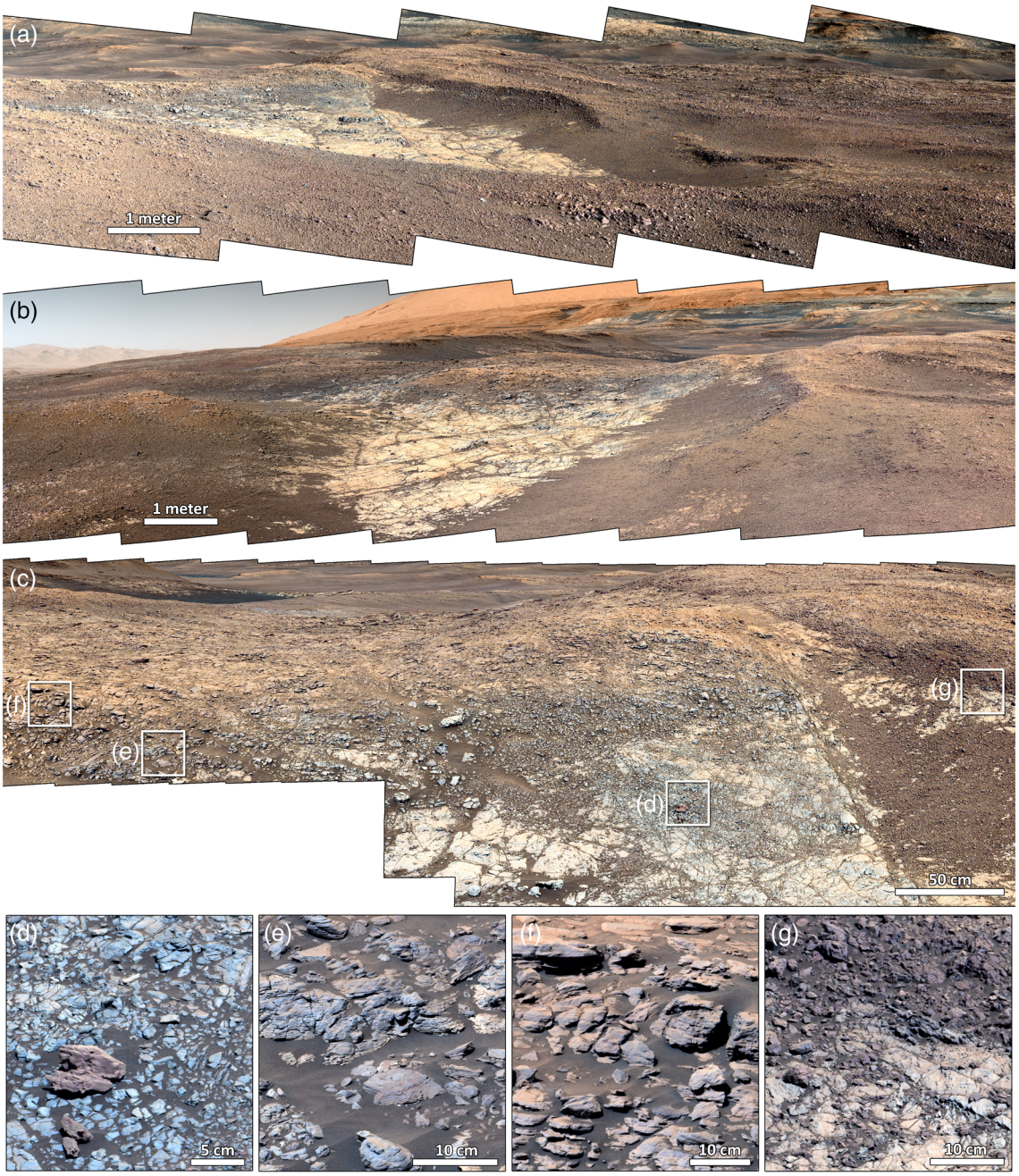

Figure 6. View of the transition between red and gray Jura bedrock as exposed in "Region E" on VRR; see Figure S1 for viewshed. (a–c) Mastcam L0 mosaic landscape views show that the dusty gray bottom of the depression is surrounded by rough textured outcrops that vary from larger blocks to smaller rubble, with a corresponding darkening in color from light red to purple due to diminishing dust cover (mcam10062, mcam10074, and mcam10081). (d–g) Zooms of (c) showing detailed changes in texture and color. See also Figures 11 and 12 for additional views and spectra of the area near (g) (target "Bowmore"). White bars indicate approximate scale in foreground for reference. Viewshed for (a) is shown in Figure S1.

overall dark overall color and abundant gray patches together are the diagnostic character of the Jura member in the orbital data. However, the gray patches do extend into the Pettegrove Point member, as can be seen in Figure 1d, although their reduced contrast compared to the overall brighter Pettegrove Point bedrock makes them more difficult to discern in that unit. This observation was confirmed on the ground, as Mastcam images show small gray patches in some locations within the Pettegrove Point member, including near the ST drill target (Figure 4d).

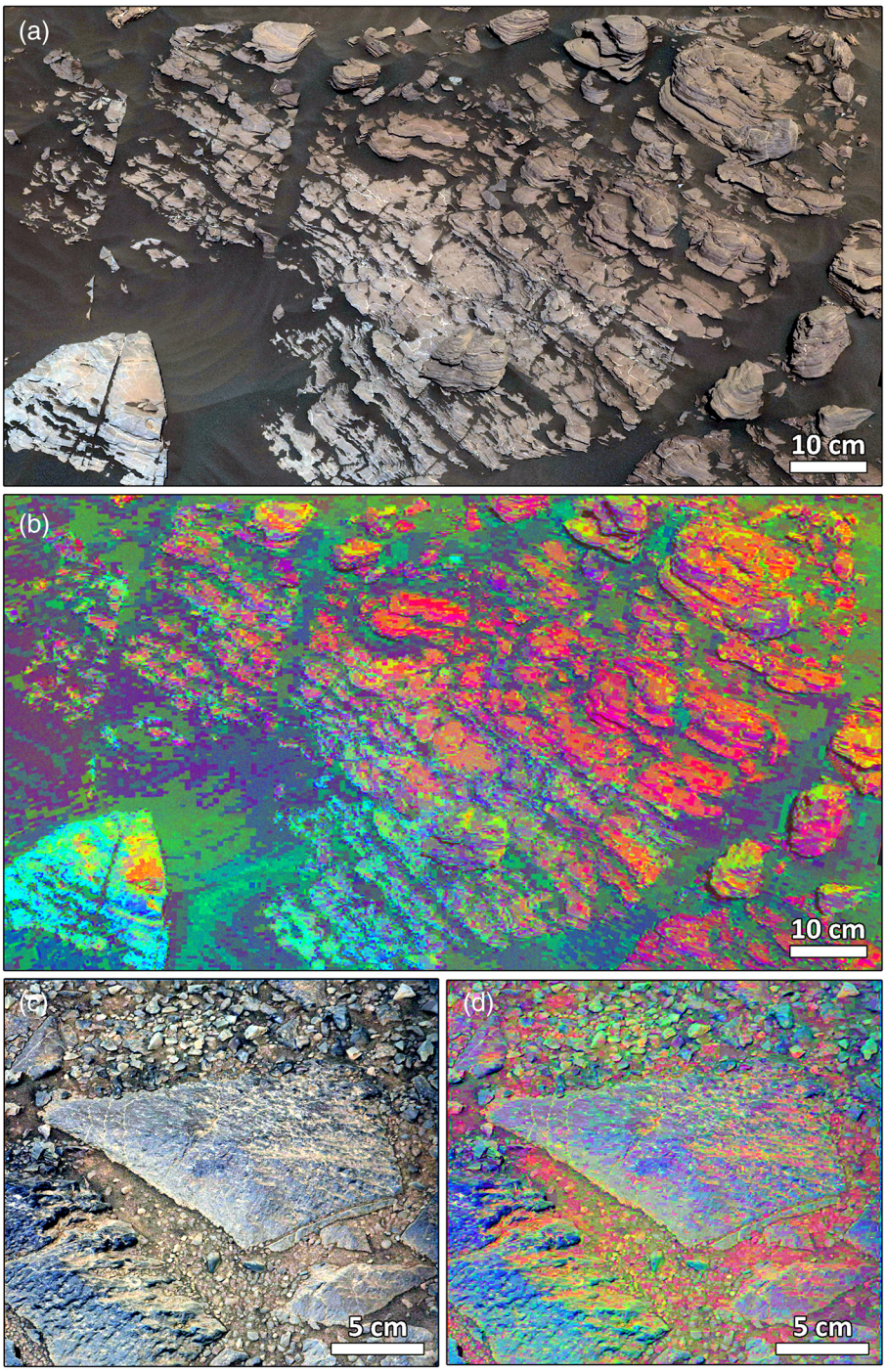

Figure 7. Detailed views of mottling in the transition zone between red and gray Jura bedrock. (a) Assynt outcrop L0 mosaic mcam10039 on Sol 1,923 in (a) white-balanced color and (b) decorrelation stretch (DCS). (c) Lyttleton target R0 image mcam09883 on Sol 1,889 in enhanced color and (d) DCS. In both DCS images, purple and magenta indicate red Jura, blue and green indicate gray Jura, and orange and yellow indicate dust.

4.2. In Situ Observations

On the ground, the orbital-scale color differences between the Pettegrove Point member and the red areas of the Jura member appear to correlate with a change in surface texture across the ridge. The boundary between the members is typically marked by the Flodigarry facies and often exhibits a steeper slope and a more broken-up texture at the contact compared to the relatively smooth and flat mudstones of the

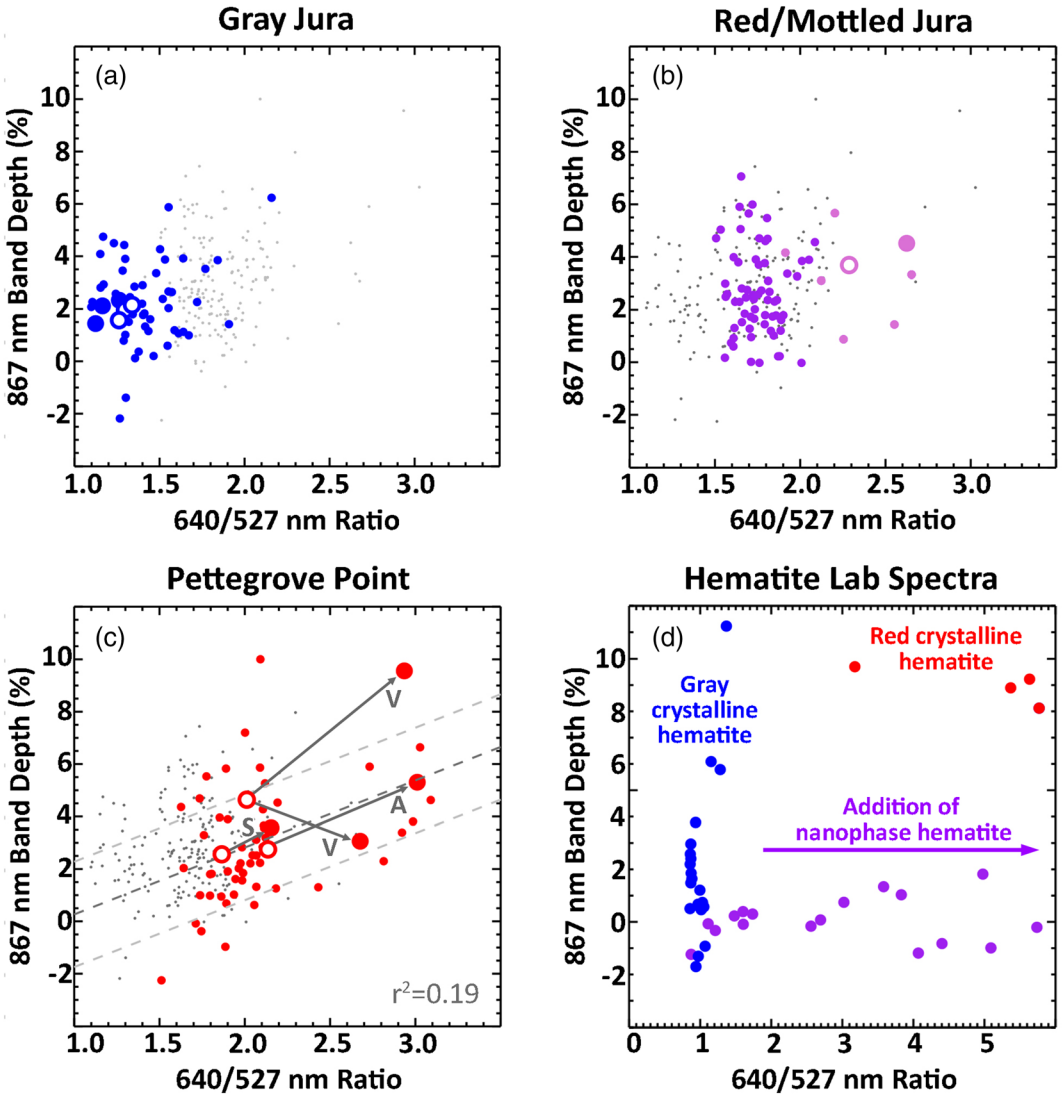

Figure 8. Comparison of Mastcam ferric spectral parameters for VRR targets, split up by unit. Gray points on all plots indicate all Mastcam bedrock spectra. Large points and circles indicate drill tailings and DRT spots, respectively, as shown in Figures 10–14. (a) Gray Jura targets, (b) red/mottled Jura targets (pink points indicate Rock Hall), and (c) Pettegrove Point targets (V and S indicate Voyageurs and Stoer). Dashed lines indicate linear fits to colored points shown along with one RMS error envelopes and labeled with R^2 values. (d) The same spectral parameters for hematite laboratory spectra convolved with Mastcam band passes, including gray and red crystalline hematite of various grain sizes (blue for specular/microplaty hematite and red for 0–10 μm red hematite; Clark et al., 2007; Lane et al., 2002) and various concentrations of nanophase hematite suspended in alumina and silica matrices (purple; Morris & Lauer, 1990). See Figure S2 for similar plots for ChemCam passive spectra.

Pettegrove Point member (Figures 4a–4c; see also Figure 10; Edgar et al., 2020). A similar broken-up and rubbly texture is common throughout red Jura bedrock but is less common in gray Jura bedrock (Figure 2; see also Figures 11–14). This difference in texture could enhance the overall brightness of smooth surfaces common on Pettegrove Point and gray Jura bedrock. However, we also observe clear differences in bedrock color and brightness in Mastcam landscape images (e.g., Figure 2) that cannot be attributed to texture alone.

Differences in bedrock colors on VRR are most apparent when comparing workspace images of bedrock cleared of most dust by the DRT, as shown in Figure 5 and quantified in section 5. The DRT spot on the DU target in the Blunts Point member displays the bright red/orange color characteristic of prior Murray targets (Wellington et al., 2017); however, no VRR DRT spots show this same color. DRT spots in the Pettegrove

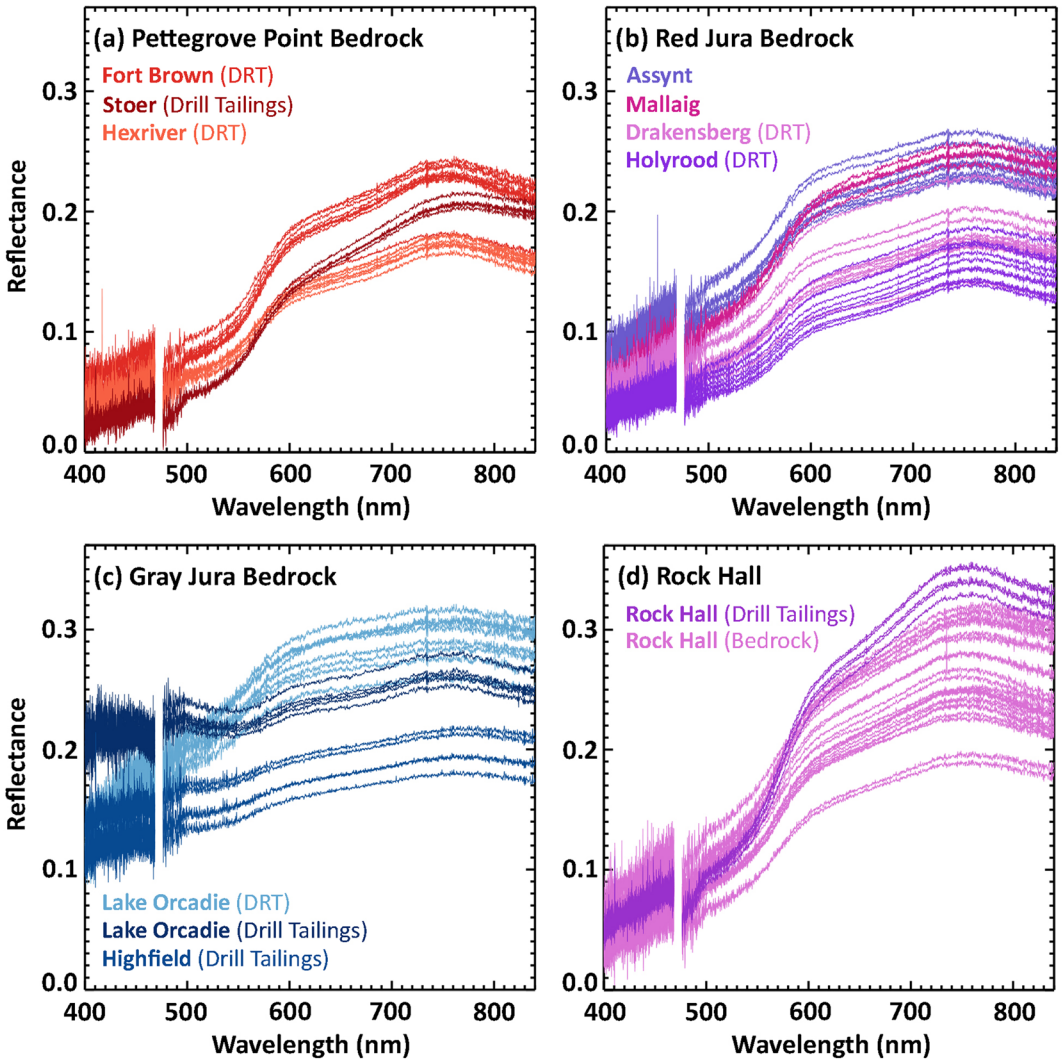

Figure 9. ChemCam passive spectra of representative bedrock targets overlapping with Mastcam targets shown in Figures 10–14, split up by unit.

Point member range from intense and homogeneous dark red colors to heterogeneous combinations of light blue/purple colors. The ST target is a light blue/purple end-member along this trend, perhaps correlating with grayer patches observed in the Pettegrove Point member from orbit. Viewing geometry and atmospheric dust do affect apparent color; however, these general color differences are apparent regardless of time of day or atmospheric opacity.

Red Jura bedrock shows a similar overall range of colors, but as discussed in section 5.2, red Jura targets exhibit slightly muted red/blue ratios, leading to generally darker and more purple colors. Local color heterogeneity in red Jura bedrock is largely in the form of smaller-scale light blue patches that may be specular reflections or calibration artifacts on these unusually light-toned surfaces (Wellington et al., 2017). Some isolated extremely red outcrops dot the surface of the Jura member (center right in Figure 2a) and occasionally occur as red cobbles on other Jura outcrops (red cobbles in Figure 13, HF target image).

On drilling, all Pettegrove Point targets take on redder hues, as does RH, the one red Jura drill target. These qualitative color changes are supported by quantitative spectral differences, as discussed in section 5. The drill tailings for the ST target are similar in color to the DU target (brown vs. red-brown, respectively; Figure 5), even though the ST bedrock is a lighter blue/gray. One possibility is that drilling is a proxy for a geologic "scratch test" and that these color changes are due to the presence of fine-grained hematite (e.g., Schwertmann, 1993). This would require that drilling increased the surface area of the hematite,

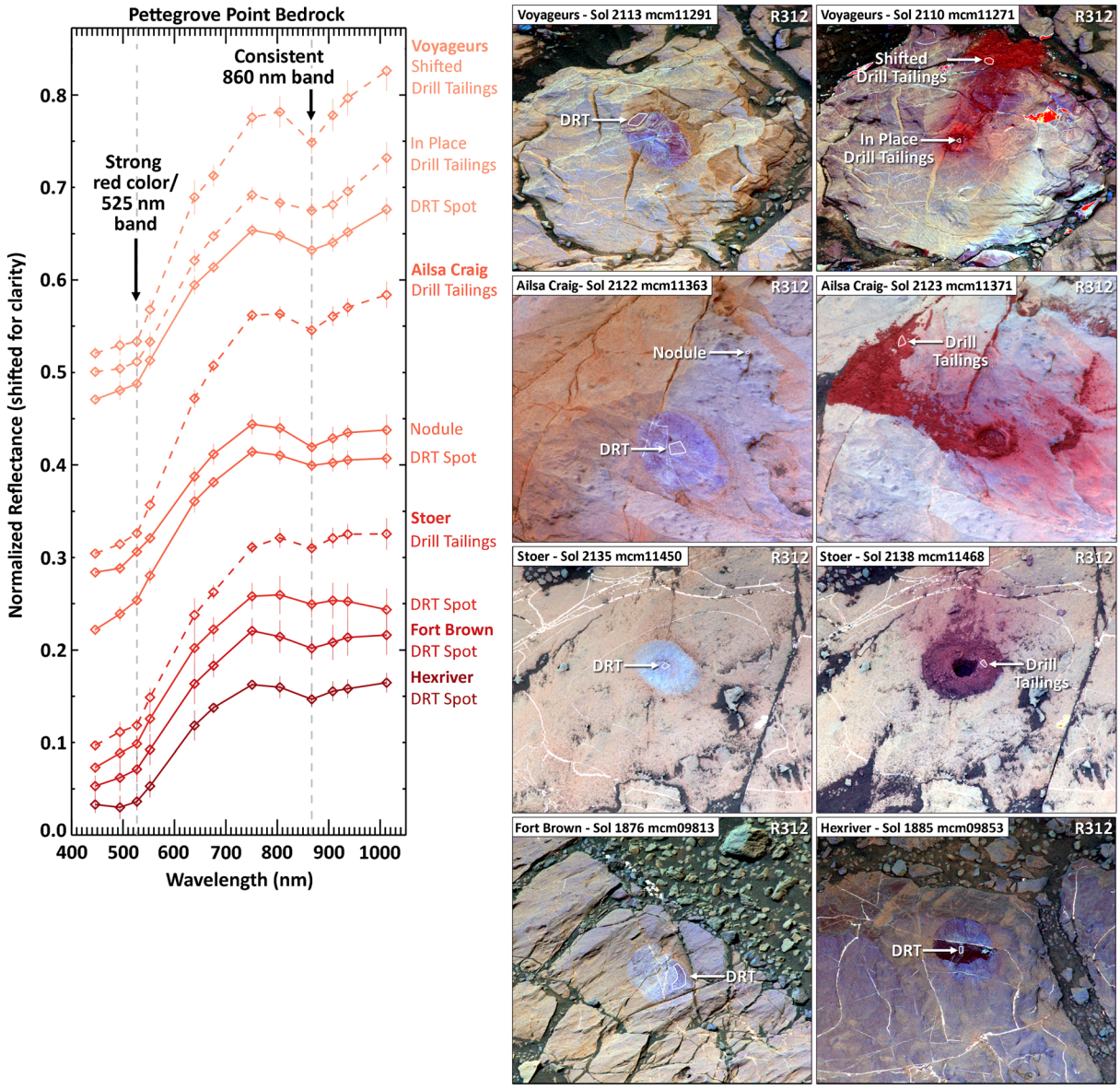

Figure 10. Pettegrove Point bedrock consistently exhibits strong red slopes, as well as 525 and 860 nm absorption bands consistent with crystalline and fine-grained red hematite. (left) Mastcam spectra, where solid lines indicate spectra from bedrock brushed by the dust removal tool (DRT) and dashed lines indicate spectra from drill tailings from aborted (Voyageurs and Ailsa Craig) and successful (Stoer) drill targets. Spectra are averaged within one contiguous ROI, stacked for clarity, and shown with error bars indicating one standard deviation within the ROI. (right) Mastcam R312 images of the targets, stretched to enhance local color diversity. White outlines indicate ROIs.

either by decreasing grain size or by liberating fine-grained hematite from other more coherent forms like coatings or clusters. Color changes from purple to red upon grinding have been observed in terrestrial rocks with clusters of smaller hematite grains (Torrent & Schwertmann, 1987). This interpretation is consistent with CheMin crystalline hematite detections across the Blunts Point member and VRR (e.g., 14.7% in ST; Rampe et al., 2020).

In contrast, gray Jura bedrock displays a relatively uniform bright blue-gray color that shows up as bright blue in the stretches in Figure 5. Some targets do show some heterogeneity with light purple streaks or patches, but these are muted and only apparent in harsh color stretches. Upon drilling, gray Jura targets do not redden and instead show a uniform gray to blue color that is similar to the most dust-free bedrock. Given that crystalline hematite was detected in high abundances in the HF drill sample (8.5 wt.%; Rampe et al., 2020), the lack of reddening is not due to a lack of hematite. Instead, this suggests that the drilling

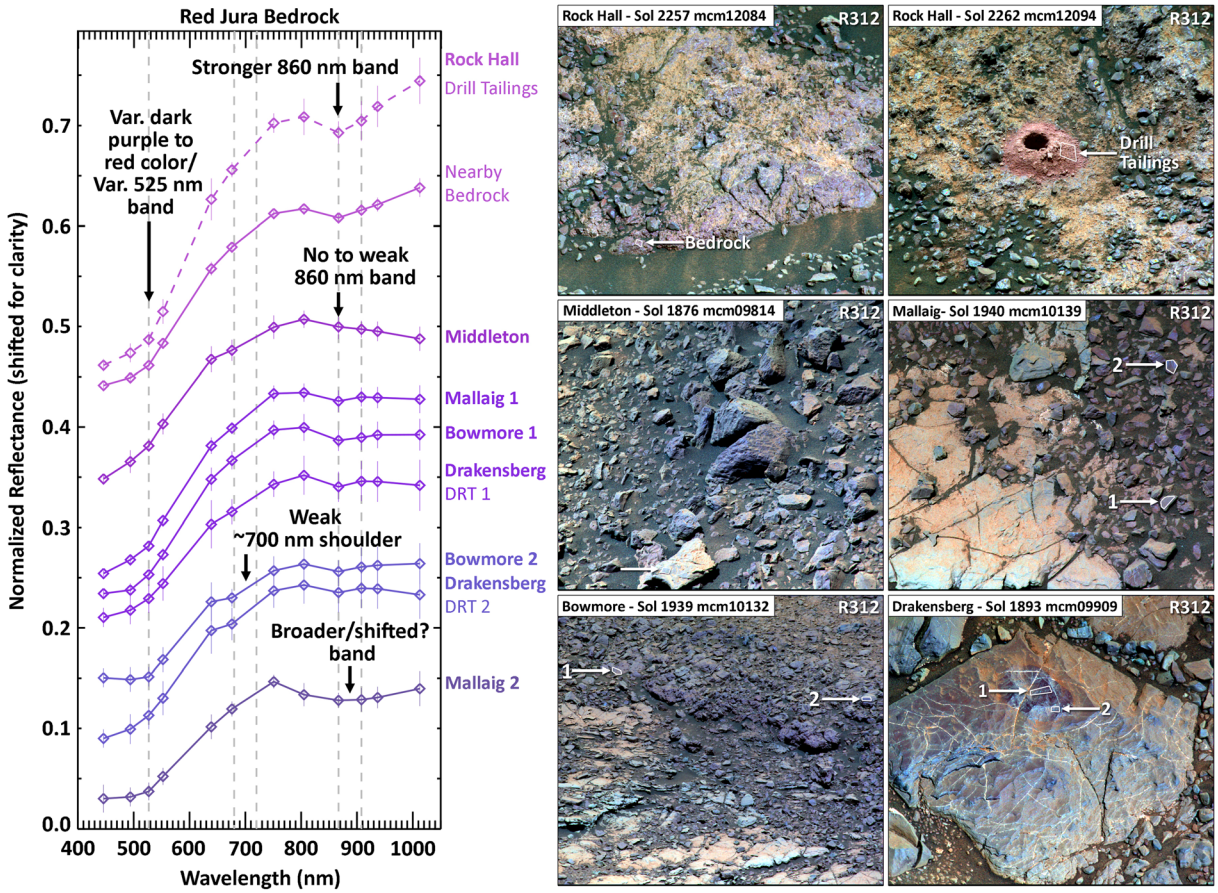

Figure 11. Red Jura bedrock is sometimes spectrally similar to Pettegrove Point bedrock but is more variable overall, including absorptions near ~700 and ~900 nm. Spectra with long-wavelength upturns and strong 860 nm bands like the Rock Hall drill target are rare, suggesting that this target may not be representative of typical red Jura bedrock. (left) Mastcam spectra, where solid lines indicate relatively dust-free bedrock and bedrock brushed by the DRT and the dashed line indicates drill tailings from Rock Hall. Spectra are averaged within one ROI, stacked for clarity, and shown with error bars indicating one standard deviation within the ROI. (right) Mastcam R312 images of targets, stretched to enhance local color diversity. White outlines indicate ROIs.

process itself does not create fine enough particles to cause reddening (0–10 μm; Morris et al., 1989) and that reddening or lack thereof upon drilling is related to properties of the hematite in the bedrock, as discussed in more detail in section 6.2.

4.3. Relationships Between Red and Gray Bedrock

The transition between gray and red/purple bedrock is most apparent in the Jura member, where decameter-scale gray patches are common. In some locations, the color units are separated by a sharp transition from purple to gray (e.g., sharp transition left of center in Figure 2d), which also sometimes corresponds to a change in surface texture from purple blocky outcrops to the gray smooth and flat surfaces on the floors of the bright depressions in the Jura member (sharp transition right of center in Figure 2d). In other locations, the color transition is gradual and occurs separately from texture (Figure 2c). Some gray smooth floors of the depressions include or are partially ringed by blocky outcrops of bluer/grayer rocks (Figure 6c). These outcrops are similar in texture to broken-up red Jura but exhibit colors closer to the gray patches, often including some purple mottling. Areas above the blocky areas in outcrop gradually transition from red to gray.

A prime example of the sharp versus more gradual boundaries is shown in Figure 6, where the center of the mosaic (Figure 6c) shows a large layered blocky outcrop that transitions from red (Figure 6f) to mottled blue/purple colors (Figure 6e) before transitioning into the smooth gray floor (Figure 6d). However, the layered mottled to red outcrop is overlain on the right by a more broken-up, dark purple unit, and farther to the

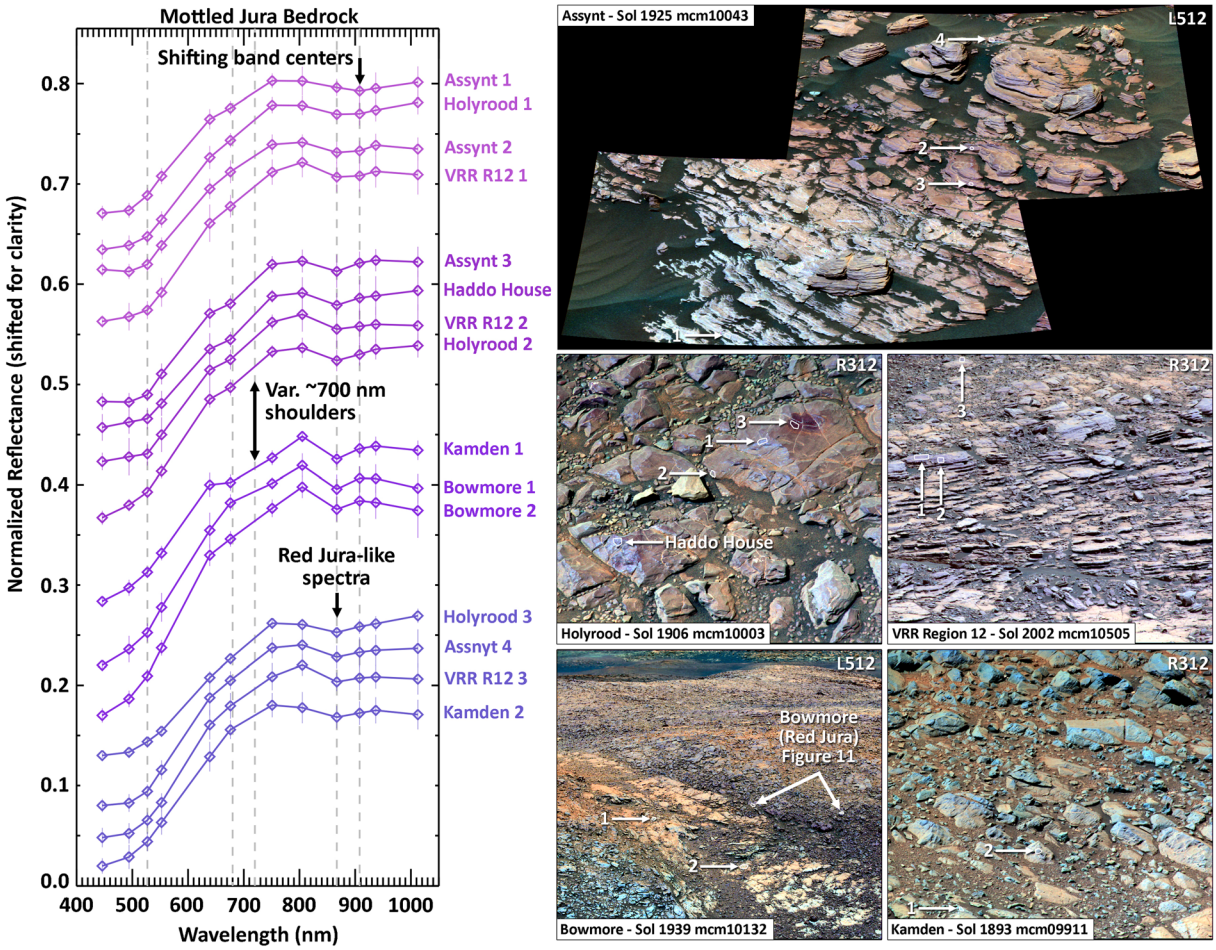

Figure 12. "Mottled" Jura bedrock at the transition between red and gray Jura bedrock exhibits significant spectral variability at small scales (e.g., within individual blocks), including flattening or shoulders in the ~700 nm region and longer wavelength ~900 nm bands. (left) Mastcam spectra from relatively dust-free bedrock targets—no multispectral images were acquired of DRT or drill targets in these regions. Spectra are averaged within one contiguous region of interest (ROI), stacked for clarity, and shown with error bars indicating one standard deviation within the ROI. (right) Mastcam enhanced-color R312 or L512 images of workspace targets corresponding to spectra on left, stretched to enhance local color diversity. White outlines indicate ROIs for each average spectrum.

right, this unit also forms a sharp boundary with the smooth gray floor (Figure 6g). These changes in color and texture within the Jura member do not appear to correspond to changes in sedimentary facies (Edgar et al., 2020), but the different textures help to enhance color differences across the unit.

In areas with gradual color transitions, the transition occurs not as a gradation in bulk color but instead as gray/blue mottles that increase in density from red Jura into the gray. This heterogeneity is apparent in the Assynt outcrop in Figure 7a, where these heterogeneities occur as approximately centimeter-scale blue mottles, which increase in frequency toward the gray regions. This is emphasized in the DCS of the Assynt outcrop in Figure 7b, where red Jura is magenta to purple, gray Jura is green to blue, and the intermediate areas show a mottled pattern of the two colors. We have observed the mottling on rock faces at a variety of incidence and emission angles (see Table S2), as shown in the Lyttleton target in Figures 7c and 7d. This suggests that at least some of these small-scale color variations are due to variable properties of the bedrock, possibly including bulk or surficial changes in iron oxidation state, iron oxide abundance, or iron oxide grain size.

Another type of large-scale gray color zoning within otherwise red rocks was observed at "Red Cliff," a resistant outcrop on the north side of VRR within the Pettegrove Point member (discussed in more detail in section 5.5). At this location, sharp boundaries separate large patches of bright red and dark gray bedrock, and the boundaries clearly crosscut stratigraphy.

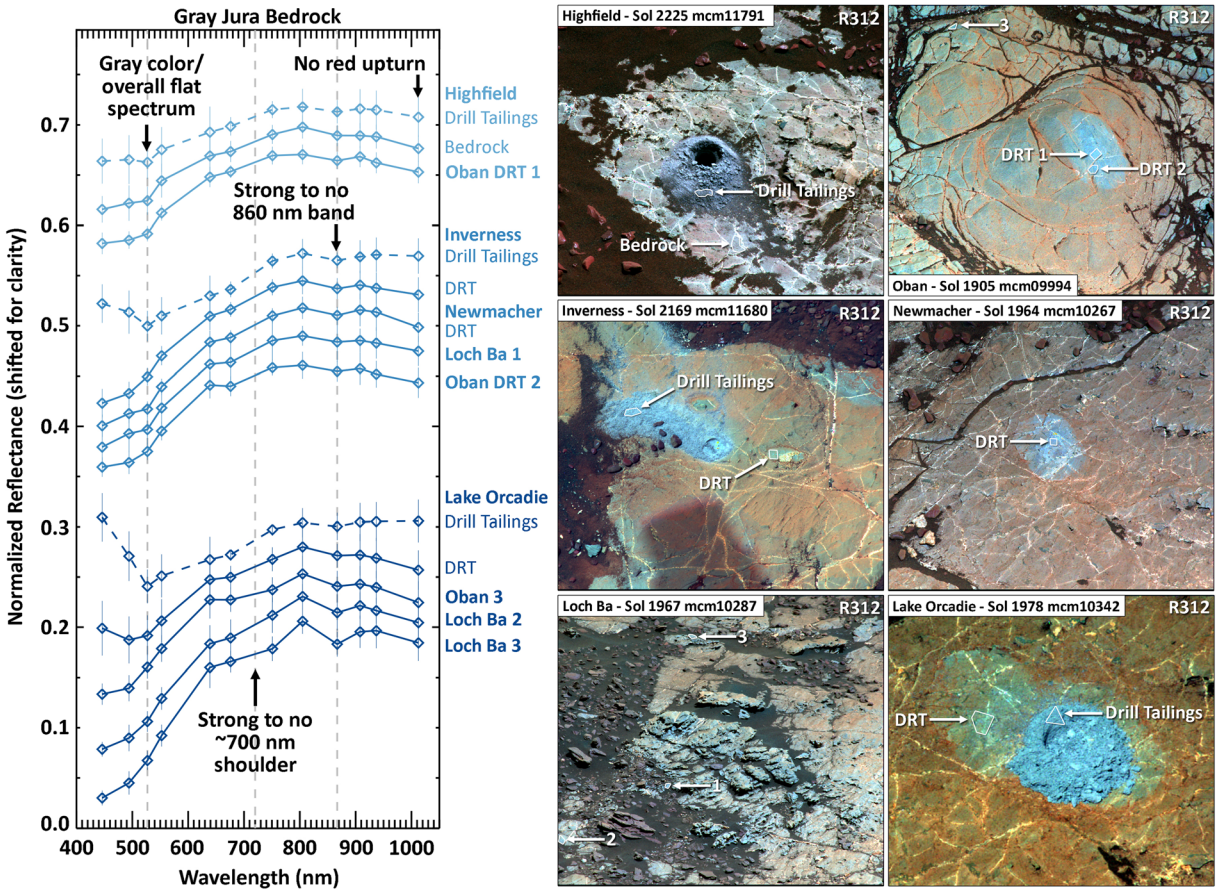

Figure 13. Gray Jura bedrock exhibits greater reflectance at short wavelengths than other VRR targets, which causes the gray color. The unit is otherwise spectrally variable, sometimes exhibiting strong ~700 nm shoulders and/or 860 nm bands near areas with very flat and featureless spectra (Figure 14). Upturns to short wavelengths may be due to reflection of the sky from specular particles. (left) Mastcam spectra, where solid lines indicate spectra from relatively dust-free bedrock and bedrock brushed by the DRT and dashed lines indicate spectra from drill tailings. Spectra are averaged within one ROI, stacked for clarity, and shown with error bars indicating one standard deviation. (right) Mastcam enhanced-color R312 or L512 images of targets, stretched to enhance local color diversity. White outlines indicate ROIs.

5. Multispectral Properties of VRR Units

5.1. Pettegrove Point

In Mastcam multispectral images, Pettegrove Point bedrock exhibits somewhat variable colors, as discussed above, but exhibits relatively consistent spectral properties. As quantified in Figures 8 and 9 and shown in Figure 10, these spectral properties include strong absorption and red slopes at short wavelengths, consistent with the red to purple color, often paired with strong absorption shoulders in the 527 nm filter. The bedrock spectra exhibit peaks below 800 nm and almost always exhibit absorption bands centered near 867 nm, although the strength of these bands varies considerably (~2–9% band depth) even when comparing DRT targets (Figure 11). Most bedrock spectra exhibit flat to red slopes beyond 800 nm, but a few (e.g., ST DRT in Figure 11) do exhibit weak downturns. These latter spectra also tend to exhibit weaker 867 nm absorption bands. These spectral properties are broadly consistent with fine-grained (red) crystalline hematite, which exhibits bands centered near 550 and 867 nm and strong red/blue ratios (Figure 3b; Morris et al., 1985). As shown in Figure 8, the 867 nm band depth and the red/blue ratio show some correlation in the Pettegrove Point member ($R^2 = 0.31$, although removing drill tailings reduces the correlation coefficient to 0.15). This relationship is potentially consistent with variations in the abundance of fine-grained crystalline hematite (<10 μm). In contrast, coarser hematite grain sizes or decreasing crystallinity do not appear to cause this same relationship (blue and purple points in Figure 8d). Changes in the abundance of ferric phyllosilicates may also be affecting the 860 nm band depth, as predicted for other members in the Murray

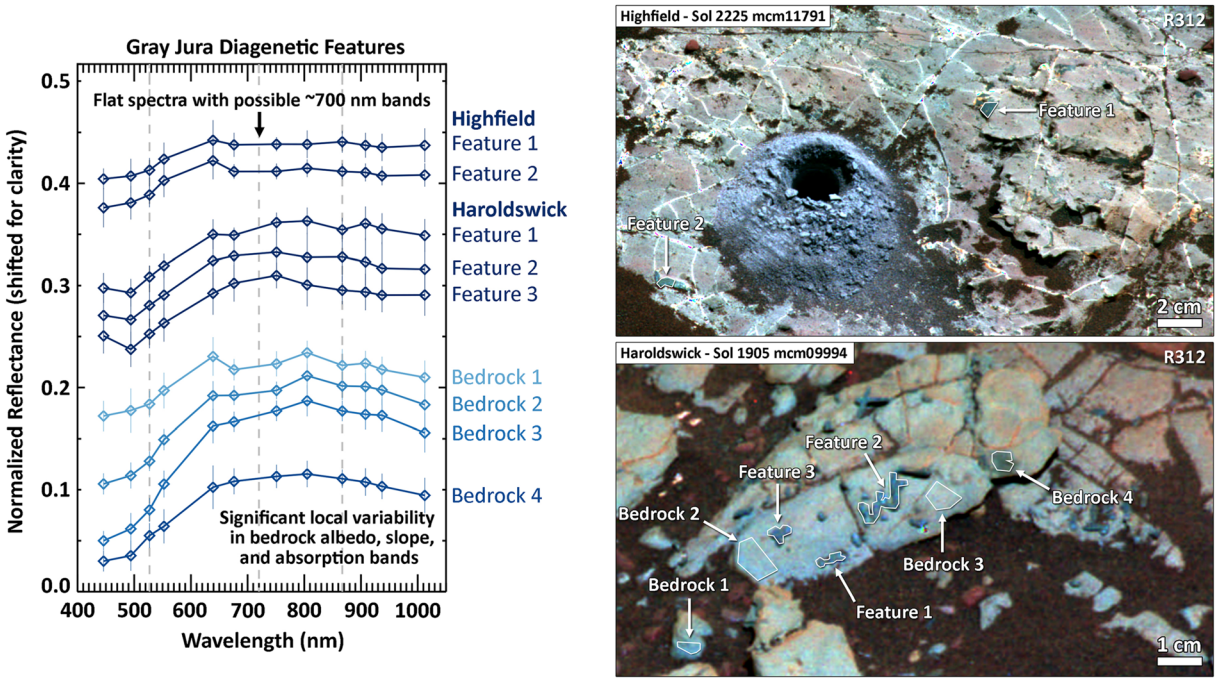

Figure 14. An example of significant local spectral diversity common in gray Jura bedrock. Dark linear to curvilinear features are interpreted as diagenetic in origin and exhibit dark and relatively flat spectra that sometimes show ~700 and 860 nm absorption bands. The high density of these features in the Haroldswick area is accompanied by local variability in bedrock albedo and spectral properties. (top) Mastcam spectra from relatively dust-free bedrock targets. Spectra are averaged within one contiguous ROI, stacked for clarity, and shown with error bars indicating one standard deviation. (bottom) Mastcam enhanced-color R312 or L512 images of targets, stretched to enhance local color diversity. White outlines indicate ROIs.

formation (Jacob et al., 2020), but are unlikely to be responsible for the color changes in bedrock and drill tailings observed in the Pettegrove Point member.

Drill tailings at Pettegrove Point targets ST, Ailsa Craig, and Voyageurs show an overall redder color corresponding to a higher red/blue ratio as well as deeper 867 nm bands when compared to the DRT spot prior to drilling (Figures 5 and 8). The drill tailings do show some variability, as the in-place drill tailings at Voyageurs exhibit a deep and broad 867 nm band (3% band depth) similar to the DRT target, but the tail of shifted drill tailings shows a stronger red slope at all wavelengths, a greater red/blue ratio, and a narrower and deeper 867 nm band (4.5% band depth). This may be due to grain-size segregation of the drill tailings during a wind event or grain flow down a local slope during the percussive action of drilling, possibly resulting in a lag of coarser grains in the in-place drill tailings. While both targets are spectrally consistent with hematite, the strong increase in both band depth and slope together in the shifted drill tailings is more consistent with laboratory spectra of fine-grained red crystalline hematite, while the in-place drill tailings are more consistent with nanophase hematite or other poorly crystalline iron oxides or oxyhydroxides (Figure 8; Morris et al., 1985; Morris & Lauer, 1990). Thus, both of these types of hematite are likely present within Voyageurs and the Pettegrove Point member more broadly.

5.2. Red Jura

"Red" bedrock targets in the Jura member exhibit more spectral variability than Pettegrove Point targets. These areas show an overall purple color with some variability in color and tone, and these differences are related to quantitative spectral differences. Overall, Mastcam red/blue ratios in red Jura targets are on average slightly lower than in the Pettegrove Point member (median of 1.76 vs. 1.96), consistent with a subtle darkening to a more purple color in the Jura member (Figure 8). Some red Jura targets are spectrally similar to Pettegrove Point bedrock (Mallaig 1 group in Figure 11), with relatively strong red/blue ratios and moderate to weak 867 nm absorption bands. Isolated patches of extremely red materials within the Jura member (e.g., center right in Figure 2a) were not imaged with the full set of multispectral filters; however, bright red cobbles that we infer to be sourced from these areas were often imaged on other Jura member

outcrops (e.g., red cobbles at lower left in Figure 13, HF image). These cobbles tend to exhibit especially strong crystalline red hematite signatures.

Unlike Pettegrove Point targets, the spectral properties of red Jura targets can vary significantly, within the same outcrop or even within the same DRT spot. Some targets exhibit much weaker red/blue ratios (Bowmore 2 and Mallaig 2 in Figure 11) and some show weak shoulders near ~700 nm (Bowmore 2 and Drakensberg DRT 2). In addition, some spectra do not show any 867 nm band at all (Middleton), and others show anomalously broad ~867 nm bands that may be shifted to slightly longer wavelengths (Mallaig 2), perhaps consistent with the presence of other ferric iron-bearing minerals like clays or oxides.

Red Jura targets show no correlation between 867 nm absorptions and red/blue ratios ($R^2 = 0.002$; Figure 8). Variability in the strength of the 867 nm band without clear variability in the strength of the short-wavelength red slope could be related to crystallinity of the iron oxide, as poorly crystalline iron oxides like nanophase hematite and ferrihydrite can exhibit a strong red slope but weak to no 867 nm bands (Figure 3b; Morris et al., 1989, 1993).

The only drill attempt in red Jura bedrock was completed at RH; however, the spectra of the RH bedrock and drill tailings are anomalous compared to other red Jura targets. RH bedrock and drill tailings spectra show strong red/blue ratios (~2–2.6), moderate to strong 867 nm bands (~3–4% band depth), and red slopes continuing to long wavelengths (Figures 9 and 11). These properties stand in contrast to the overall weaker bands and slopes in other red Jura targets in both Mastcam and ChemCam data (Figures 8 and S2). Compared to the surrounding purple bedrock, the drill tailings exhibit stronger red slopes and 867 nm bands that are consistent with their brighter red color. Together, all of these properties suggest a greater spectral contribution from fine-grained crystalline hematite than in other red Jura targets. CheMin data show that the dominant iron oxide in RH is akaganeite with minor hematite (Rampe et al., 2020), although the spectra are still dominated by the small amount of hematite present, and no akaganeite signatures are apparent. Along with the observation that RH exhibits some unusual physical characteristics compared to other VRR outcrops (e.g., large polygonal blocks surrounded by sediment-filled moats, and soft and thus drillable surface), the overall spectral distinctiveness of RH suggests that the mineralogy of RH may not be representative of red Jura bedrock.

5.3. Mottled Jura

The transitional or "mottled" region between red and gray regions in the Jura member is spectrally similar to red Jura regions but shows even more small-scale spectral variability. No drill attempts were made within these transitional zones due to their broken-up texture, and only one DRT spot was targeted with multispectral images (Holyrood 3 in Figure 12), so the spectral interpretations here are largely based on relatively dust-free bedrock.

As in red Jura areas, some local areas within the mottled Jura show Pettegrove Point-like spectra (Holyrood 3 group in Figure 12), but a much larger proportion of the outcrops show other spectral properties as well. In particular, weak to moderate shoulders near ~700 nm are more prominent (Assynt 3 and Kamden 1 groups) and are often but not always associated with more blue surfaces. Some spectra with ~700 nm shoulders or flattening also show stronger 867 nm bands (Kamden 1 group), but there is no clear correlation between the two spectral features ($R^2 = 0.03$). Finally, some spectra within the mottled regions show variability in the position of the 867 nm band (Assynt 1 group), perhaps consistent with significant quantities of other ferric iron-bearing oxides or clays relative to hematite. Fine-grained hematite is such a strong pigment that other ferric minerals must be present at high abundances to shift the band center (e.g., a shift to ~900 nm band centers requires goethite:hematite ratios of 3:1; Townsend, 1987).

The "mottling" in visible color is consistent with variable short-wavelength absorptions and slopes observed throughout the red/gray transitional regions, which also show no clear correlation with other spectral features. However, even relatively gray bedrock within the transition zone still shows weak to moderate 867 nm bands (e.g., Kamden and Bowmore in Figure 12).

5.4. Gray Jura

"Gray" bedrock targets in the Jura member exhibit the most spectral variability of any VRR color unit. Nearly all targets have significantly lower red/blue ratios (~1.1–1.9, median 1.35) compared to red Jura or

Pettegrove Point targets (Figure 8), consistent with their gray/blue color. Some targets exhibit extremely flat spectra throughout the VNIR (HF and Oban DRT 1 in Figure 13). These spectral differences compared to other VRR targets are most apparent in the unnormalized ChemCam spectra shown in Figure 9. However, even these spectrally flat targets still often exhibit very weak bands near 867 nm. This suggests that at least some crystalline hematite is present but that red fine-grained hematite is unlikely to be present at more than trace abundances. Coarser-grained hematite (tens or hundreds of micrometers) loses the distinctive red character of <10 μm hematite but can still cause a band at 867 nm (Figures 3 and 8; Lane et al., 2002). In addition, some visibly gray targets do still exhibit strong red/blue ratios and 867 nm bands (Loch Ba 2/3), suggesting significant variability in the crystallinity, grain size, and/or abundance of hematite within gray Jura bedrock.

Most other spectra of gray Jura targets exhibit a feature ranging from a flattening to a deep shoulder near ~700 nm (Inverness and Lake Orcadie groups in Figure 13), similar to but often stronger than similar spectral features observed occasionally in red Jura targets and more commonly in the mottled Jura. In general, this spectral feature appears to increase in frequency and strength within the Jura member as a function of color, from the red regions, through the mottled regions, and into the gray regions, and the depth of the shoulder is somewhat correlated with bluer spectral slopes (lower red/blue ratios) in both red and gray Jura targets (R^2 = 0.25/0.19 in gray/red Jura targets compared to R^2 = 0.06 in Pettegrove Point targets). The exact center of this shoulder or band is not well resolved in the multispectral data and may be variable. Several Fe-bearing minerals exhibit shoulders or absorption bands between 650 and 750 nm, including ferric- and mixed valence iron-bearing phyllosilicates (Fe^{3+}-smectite and Fe^{2+}-smectite, chlorite, and celadonite in Figure 3) as well as some iron oxides and oxydroxides (goethite, lepidocrocite, and some varieties of crystalline hematite in Figure 3b). However, of these, only Fe^{2+}-bearing phyllosilicates and certain varieties of gray crystalline hematite (microplaty hematite; Lane et al., 2002) also exhibit blue spectral slopes at short wavelengths, and only hematite is potentially consistent with CheMin results (Rampe et al., 2020). Thus, it is possible that coarse-grained and perhaps microplaty-textured hematite is present within both red and gray Jura bedrock. However, this spectral feature is quite spatially variable and is not strong in any drill tailings targets, so other minerals not detected by CheMin cannot be ruled out. Several gray Jura surfaces and all drill fines also show sharp upturns to short wavelengths, which may be due to reflection of the sky from specular particles (potentially including the microplaty hematite discussed below).

Dark diagenetic features are abundant in gray Jura bedrock (Bennett et al., 2020; David et al., 2020; L'Haridon et al., 2020; Tinker et al., 2019) and, in some locations, are large enough to be resolved by Mastcam multispectral imaging. These features are densely populated in and around the HF drill target and exhibit remarkably flat spectra with limited short-wavelength absorptions, no 867 nm absorption, and a possible band or shoulder near ~700 nm (Figure 14). At the Haroldswick area, which is near the Oban DRT target shown in Figure 5, clusters of large diagenetic features with linear to sinuous morphologies exhibit slightly less flat spectra with variable weak bands near ~700 and 867 nm (Figure 14). The bedrock surrounding these features is also highly variable, exhibiting both bright and dark patches with flat spectra (Bedrock 1 and Bedrock 4 in Figure 14) and some areas with strong ~700 nm bands. These absorption bands are consistent with microplaty hematite, a specific textural variety of gray hematite, and their variability within the bedrock and diagenetic features could reflect both variations in hematite abundance and grain texture. In support of this interpretation, ChemCam investigation of dark diagenetic features in gray Jura bedrock suggests that they are consistent with gray hematite (L'Haridon et al., 2020), both in their chemistry (very high FeO abundance without hydrogen enrichment, depletion in all other cations, and lack of volatile elements such as S or Cl) and texture (euhedral crystals with hexagonal faces).

The overall flat spectra observed in both the bedrock and diagenetic features in gray Jura bedrock could be due to the presence of iron oxides with flat to blue-sloped spectra, which include microplaty hematite (Lane et al., 2002) but also magnetite (Morris et al., 1985). Magnetite is present at the CheMin limit of detection (<1%) in all VRR samples except RH, and the peak of the flat spectra near 800 nm is consistent with magnetite; however, hematite is much more abundant (8.5% in HF; Rampe et al., 2020), and microplaty hematite may explain the presence of shoulders near ~700 nm. Both magnetite and gray hematite retain these spectral properties even upon grinding (Figure 3; Morris et al., 1985; Lane et al., 2002) and thus could be consistent with the lack of reddening observed in gray Jura drill targets (Figures 5 and 11). Finally, as the flattening is also observed in light-toned bedrock, bright materials like silica or sulfates are likely enhancing flattening

and albedo in the light-toned bedrock (Morris & Lauer, 1990). While sulfate abundances in HF from CheMin analyses are not appreciably higher than other drill samples (~3%; Rampe et al., 2020), silica is consistent with 4% opal CT in the crystalline component and 65% significant silica in the amorphous component of HF, as well as an increase in Si and Al in Alpha Particle X-ray Spectrometer (APXS) measurements of gray Jura bedrock in general (Thompson et al., 2020).

5.5. Red Cliff

Red Cliff, the large outcrop on the north side of VRR in Pettegrove Point bedrock, shows clear regions of red and dark gray bedrock separated by apparent sharp color boundaries. The relatively dust-free cliff has high spectral contrast, and red areas show strong 867 nm bands and red/blue ratios (Figure 15) similar to other Pettegrove Point spectra (Figure 10) and consistent with red hematite. The gray areas exhibit spectral properties similar to the mottled Jura or more ferric portions of gray Jura bedrock (Figures 12 and 13), including weaker red/blue ratios and 867 nm bands, and variable 700 nm shoulders or flattening, consistent with coarse hematite.

6. Discussion

Mastcam images and spectra allow us to place detailed mineralogical assemblage predictions from CheMin that are derived from single centimeter-scale samples in context within the larger stratigraphic and geologic context. In particular, Mastcam can provide information on the spectral variability or consistency of iron-bearing minerals and mineraloids across outcrops and bedrock units. Understanding the spatial distribution of key environmental indicator minerals provides important constraints on the alteration processes that may have produced them.

However, Mastcam spectral information can only provide insight into a subset of minerals (Figure 3) and is limited by the nonlinearities inherent to VNIR spectra. In particular, absorptions due to hematite can dominate this region even at very low abundances, especially when the hematite is fine grained (e.g., Morris et al., 1985; Morris & Lauer, 1990; Townsend, 1987). Because of these effects, hematite is the main contributor to Mastcam spectral signatures across VRR, even though the actual abundance of crystalline hematite varies substantially across the three VRR samples analyzed by CheMin (Rampe et al., 2020)—14.7% hematite in ST (Pettegrove Point), 2.9% in RH (red Jura), and 8.5% in HF (gray Jura). Other minerals detected on VRR that could be spectrally detectable by Mastcam include pyroxene (3–9%), akaganeite (0–6%), magnetite (0–0.5%), jarosite (0–2%), and ferric smectite (5–13%); however, these minerals can likely all be spectrally masked by hematite (e.g., Jacob et al., 2020; Morris & Neely, 1982; Townsend, 1987).

6.1. Spectral Variability as Context for Drill Samples

Although the Pettegrove Point member shows somewhat variable color properties at the scale of individual DRT spots, hematite signatures are pervasive throughout the unit in Mastcam spectra. Thus, even though the ST bedrock exhibits lighter, grayer, or bluer colors than some other areas in the Pettegrove Point member, the fact that the spectral signatures are well in family with the rest of the unit suggests that the drill sample is a somewhat representative sample, although ST may represent one point on a broader trend of increasing hematite grain size, crystallinity, and/or abundance with increasing red color.

Within red Jura bedrock, Mastcam spectral signatures are highly variable at large and small scales. Large bright red patches within red Jura bedrock may correspond to strong crystalline hematite signatures observed in some red cobbles. At the small scale, most outcrops show centimeter-scale color and spectral variability, including many areas with notably weak short-wavelength red slopes and weak or no 860 nm bands. Some areas show completely different broadened and shifted bands. Shifts in the center of the ~900 nm band to longer wavelengths could be consistent with various iron oxides/oxyhydroxides (akaganeite, goethite, and lepidocrocite), iron sulfates (jarosite), or iron-bearing smectites (nontronite). While none of these can be ruled out based on spectral properties alone, the detection of minerals other than hematite in the ~900 nm range implies that these locations do not contain more than a trace amount of crystalline, fine-grained hematite, which would normally obscure these other spectral signatures. Together, these observations suggest significant variability in the iron-bearing mineralogy of red Jura bedrock, perhaps including significant differences in abundance of both crystalline and poorly crystalline hematite and the presence of other ferric phases.

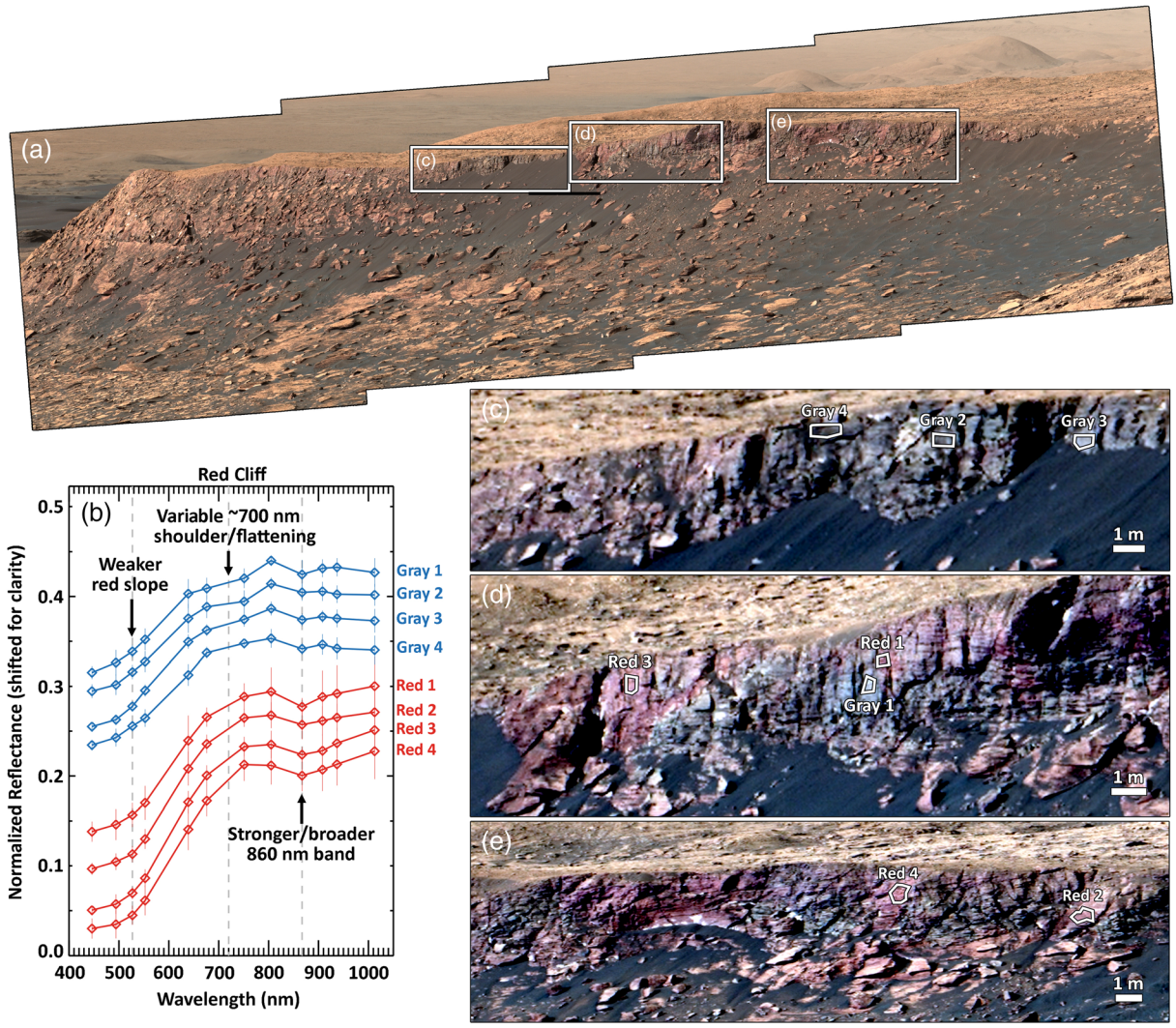

Figure 15. Red Cliff on the north side of Vera Rubin ridge, within Pettegrove Point bedrock exhibits both bright red and dark gray patches with sharp boundaries. (a) R0 Mastcam mosaic mcam10769 from Sol 2,038 in white-balanced RGB Bayer filters. Illumination from left. (b) Mastcam spectra, averaged within one ROI, stacked for clarity, and shown with error bars indicating one standard deviation. (c–e) Enhanced-color stretch of image in (a). White outlines indicate ROIs.

The interpretation that red Jura bedrock has spatially variable secondary iron mineralogy is supported by CheMin measurements of the RH drill sample mineralogy, which includes 6.0% akaganeite in addition to the relatively small amount of crystalline hematite (2.9%). The akaganeite is not apparent in the Mastcam spectra, which are dominated by crystalline hematite absorptions even at the low abundances of hematite detected by CheMin. RH is more spectrally similar to the red cobbles and possibly the bright red patches in the Jura member than to the more common weak hematite/ferric signatures throughout the rest of red Jura targets. Thus, RH may represent a compositional outlier or end-member within red Jura bedrock.

Gray Jura bedrock is also highly variable in Mastcam spectra, ranging from strong red/blue ratios to very flat spectra. Flatter spectra tend to exhibit weaker or no 860 nm bands from red crystalline hematite, and while shoulders near ~700 nm tend to be stronger within flatter spectra, flatter spectra without these shoulders are also common. The HF DRT and drill tailings exhibit flat spectra with weak to no 860 nm bands and no ~700 nm shoulder and so are representative of the brightest parts of gray Jura bedrock. Thus, the moderate hematite abundances (8.5%) in HF are also likely representative of the brightest parts of the Jura member and, because of the lack of any clear spectral signature of poorly crystalline or fine-grained iron oxides in these areas, likely also represent the total bulk hematite abundance in the bedrock.

6.2. Hematite Across VRR

Crystalline hematite signatures are common in red VRR bedrock, although they vary significantly in strength. In general, the reddest rocks with high red/blue ratios do exhibit stronger absorption bands due to red crystalline hematite at 860 nm (Figures 4 and 8). These parameters are somewhat correlated for targets in the Pettegrove Point member, suggesting that their variations may be at least partially due to variations in the abundance of red crystalline hematite within the Pettegrove Point member. In contrast, the Jura member does not exhibit a correlation between red/blue ratios and the strength of the 860 nm band. While some crystalline red hematite is likely present in red Jura bedrock, this suggests that the primary spectral variability in red Jura bedrock is related to the abundance of other ferric iron-bearing materials. A strong candidate for this other ferric material is a poorly crystalline iron oxide like nanophase hematite or ferrihydrite, which would not be detected by CheMin and exhibit a strong red/blue ratio and weak 860 nm band (Morris et al., 1989, 1993) that is more consistent with the trends observed in red Jura targets (Figure 8).

We hypothesize that the Jura member also contains coarsely crystalline hematite, as this is one explanation for the variable ~700 nm shoulder observed sporadically in red Jura targets, more often in the mottled Jura, and commonly in gray Jura bedrock; 700 nm band depths are correlated with relatively bluer slopes, both in red and gray Jura bedrock and in Jura dark diagenetic features with very flat spectra, potentially consistent with microplaty hematite, a coarsely crystalline form of hematite that notably does not change spectral properties upon grinding (Lane et al., 2002). Gray hematite with limited red or nanophase hematite and mixed with bright materials like silica could thus be responsible for the overall flattening of gray Jura spectra.

Color trends across the ridge could be consistent with changes in hematite grain size, crystallinity, or texture. The subtle color differences between the more red colors of Pettegrove Point bedrock and the somewhat darker purple colors in red Jura bedrock could be related to red hematite versus gray hematite, respectively—in terrestrial red beds and soils, similar color changes from red to purple are often attributed to coarsening of hematite grains (Schwertmann, 1993; Torrent & Schwertmann, 1987). Clustering of finer grains could also be responsible for purple colors on VRR, as terrestrial red beds and soils with clusters of hematite grains tend to exhibit more purple colors (Torrent & Schwertmann, 1987). Finally, mixing with poorly crystalline iron oxides like nanophase hematite could also be affecting the overall color, as nanophase hematite is a powerful reddening agent (Morris et al., 1993).

Color changes upon drilling may also be an indicator of hematite grain size in the bedrock. Pettegrove Point targets Voyageurs and Ailsa Craig exhibit the most intense reddening upon drilling, both based on visual inspection (Figure 5) and red/blue ratio (Figure 8). Pettegrove Point target ST and Jura target RH also show reddening upon drilling but less intensely than Voyageurs. In contrast, Jura target HF shows bluing on drilling. As all of these samples contain hematite, the lack of reddening in HF in particular demonstrates that the percussive action of the drill is insufficient to generate red hematite from gray hematite. But because reddening does occur in the other samples, drilling is affecting the properties of the hematite in the bedrock in some way.

One hypothesis to explain these color differences on drilling is that the hematite is present in a different form in the different units—for example, as coatings or cement, individual larger grains, or clusters of grains. Parry & Chan (2004) showed that oxidized Navajo Sandstones with both hematite coatings around the sand grains and pore-filling hematite masses turned pink to red on grinding to <10 micron particles, but bleached sandstones with individual ~40 micron hematite grains retained their original gray to pale orange color on grinding. Color changes from purple to red upon grinding have also been observed in terrestrial red beds dominated by clusters of smaller hematite grains (Torrent & Schwertmann, 1987). Thus, one explanation for the reddening of some of VRR rocks on drilling could be that grinding liberated red fine-grained crystalline hematite from coatings or clusters, giving it a larger surface area. This is potentially consistent with the observation of grain-size segregation of the Voyageurs drill tailings by wind or downslope kinematic sorting, which suggests that fine-grained red crystalline hematite is more abundant in the coarser size fractions of the tailings. In contrast, hematite in gray Jura bedrock may be primarily present as individual grains, which are not as susceptible to reddening upon drilling.

In summary, the spectral properties of bedrock on VRR are consistent with at least three ferric components, which we attribute to fine-grained but crystalline red hematite present as coatings or clusters, poorly crystalline iron oxides like nanophase hematite or ferrihydrite present as coatings or cement, and coarsely

crystalline gray hematite present as individual grains (tens of microns or larger). Variations in spectral properties and color within and between units on VRR are likely due to variations in the relative abundance of these three components as well as their morphology (coatings vs. clusters vs. individual grains). We hypothesize that in Pettegrove Point, bright red colors are due fine-grained crystalline hematite, which reddens and produces strong hematite spectral signatures on grinding due to liberation of the crystalline particles from coatings or cements. In the red Jura and parts of Pettegrove Point (e.g., ST), more purple colors with weaker hematite signatures that redden somewhat upon grinding are likely due to clustering of red crystalline hematite grains. All red VRR rocks likely contain some poorly crystalline iron oxides along with red crystalline hematite, perhaps in the form of a cementing agent or grain-scale coating. Spectral signatures consistent with microplaty hematite are present in reflective patches in some locations in the red Jura, commonly in the mottled Jura, and throughout the gray Jura, suggesting that coarsely crystalline gray hematite is present throughout the Jura but increases in proportion toward the gray patches. The brightest areas within gray Jura bedrock show no spectral signatures of any fine-grained hematite and are dominated by gray hematite in both the bedrock and diagenetic features. Hematite spectral signatures obscure all other spectral signatures in all areas, except for patches within red Jura bedrock that show evidence of absorption bands due to other ferric minerals (e.g., oxyhydroxides, sulfates, or smectites), and these patches are most common in the transitional regions between the red and gray Jura bedrock.

6.3. Diagenesis of VRR

Alteration and lithification of sedimentary basin strata like the Murray formation under the low-temperature and pressure conditions that dominated the majority of the upper crust of Mars is collectively referred to as diagenesis. Diagenesis is a continuum of processes from deposition through burial and exhumation but is typically divided into stages of early and burial (or late) diagenesis (e.g., Montañez & Crossey, 2018). Early diagenesis on Earth occurs during and after deposition of rocks and sediments, typically at burial depths up to hundreds of meters or even 1 km and temperatures similar to those possible at the surface (typically below ~30°C). This realm includes surface processes of weathering and pedogenesis, as well as initial burial processes of cementation, compaction, and dewatering. Late diagenesis occurs during deeper burial and results in further compaction and loss of porosity at elevated temperatures (e.g., up to 100°C for 3–4 km burial depth on Earth). Fluid movement during late diagenesis in particular is very sensitive to spatial changes in permeability and will tend to follow relatively more permeable horizons. Diagenetic histories of rocks can be very complex, as multiple fluid events commonly occur during every stage of diagenesis. Differentiating the effects of early versus late diagenesis is challenging and often requires detailed microscopic analysis of the physiochemical relationships between sediment grains and secondary minerals (e.g., Potter-McIntyre et al., 2014).

The Murray formation exhibits clear evidence for burial and later diagenesis in the form of veins and concretions. Sulfate-filled veins are hypothesized to have formed during or after burial due to hydrofracturing (cracks formed due to fluid pressure) of lithified bedrock under pressure by multiple distinct episodes of fluid flow (Caswell & Milliken, 2017; Kronyak et al., 2019; Nachon et al., 2017). Concretions of diverse morphologies are also found throughout the Murray formation and are interpreted to have formed during a series of late diagenetic events after sediment compaction and lithification (Sun et al., 2018). Hydration of Ca sulfates in the Murray formation places some limits on the temperatures experienced during burial, as the preservation of bassanite in veins suggests temperatures below 60°C (Rapin et al., 2016). However, the role of early diagenesis in the Murray formation is less clear. Sulfate within the bedrock of parts of the Murray formation may have formed during evaporative lacustrine phases (Rapin et al., 2019). The fine-grained red hematite detected throughout the Murray formation below VRR has also been hypothesized to have formed through a variety of early diagenetic mechanisms, including authigenic formation in shallow lake waters (Hurowitz et al., 2017) and during early diagenesis within the sediments by oxidizing groundwater interaction (Rampe et al., 2017).

These formation mechanisms are analogous to those proposed for fine-grained red hematite-bearing units in terrestrial sedimentary strata, which are commonly referred to as “red beds.” Hematite is typically present in red beds as coatings on grains and pore-filling cements, formed both by early subaerial or shallow water weathering under oxidizing surface conditions (Metcalfe et al., 1994; Potter-McIntyre et al., 2014; Sheldon, 2005; Van Houten, 1973) or by downward transport of oxidizing meteoric water either during

early diagenesis or later after uplift and reapproach to the surface (Johnson et al., 1997; Mücke, 1994; Walker, 1976). The hematite in "primary" red beds is formed during early diagenesis prior to significant compaction and shows more continuous hematite at both the microscopic (e.g., coatings and cements clearly formed around grains prior to compaction) and outcrop scales (e.g., uniform red coloration throughout the unit), as compared to "secondary" red beds, in which the hematite formed after lithification (Eichhubl et al., 2004; Johnson, 1976; Potter-McIntyre et al., 2014).

The three varieties of iron oxide that we suggest are prevalent within VRR—poorly crystalline iron oxides, fine-grained red crystalline hematite, and coarsely crystalline gray hematite—are also found in SEM analyses of red beds like the Moenkopi Formation in the western United States (Walker et al., 1981). In these rocks, much of the red pigment appears to be tied to the poorly crystalline component, which exhibits no crystalline structure down to the submicron scale, and is interpreted to be nanophase hematite. Micron-scale crystalline red hematite grains are also abundant, both as individual grains and as intergrown clusters or networks. These grains grade into larger individual crystals or crystal aggregates of gray hematite a few to tens of microns in size. Gray hematite is also present as martite, a specific texture formed through oxidation and replacement of detrital magnetite grains. Overall, the Moenkopi red beds examined in Walker et al. (1981) show clear evidence for many successive diagenetic events that created multiple generations of hematite coatings and grains. Based on diverse and complex associations between hematite and other diagenetic minerals, it is hypothesized that hematite was initially deposited as an early diagenetic coating but continued to form during later diagenetic alteration.

We hypothesize that alteration by oxidizing fluids (e.g., meteoric or lacustrine) was responsible for initial deposition of red crystalline hematite and nanophase iron oxides in VRR, but that additional diagenetic processes are necessary to explain the distribution of the various types of hematite on the ridge. Oxidation is more likely to be caused by near-surface fluid interactions than at depth because oxidizing fluids in basaltic aquifers are rapidly depleted of oxidants by bedrock interactions (e.g., Hurowitz et al., 2017). Abiotic oxidants in near-surface waters could include dissolved atmospheric O_2 or H_2O_2, or oxidizing species such as chlorate (Mitra & Catalano, 2019). However, this oxidation likely did not occur due to extensive top-down, open system weathering, which would have resulted in elemental enrichments that were not observed by Curiosity on VRR (Fraeman, Edgar, et al., 2020). Early oxidation under more isochemical conditions may be consistent with the lacustrine and early diagenetic alteration models proposed by Hurowitz et al. (2017) and Rampe et al. (2017). Based on terrestrial analogs (e.g., Walker et al., 1981), oxidation likely occurred through multiple oxidizing diagenetic events, and the exact timing of this process relative to sediment deposition and burial is difficult to infer from the presence of hematite alone.

Spectral differences across VRR are most easily explained through coarsening of this fine-grained hematite. Red rocks with spectra consistent with abundant red fine-grained hematite in Blunts Point grade into the slightly more purple Pettegrove Point, into the more purple Jura, and finally into gray Jura, which, in some areas, appears to be nearly or entirely depleted of poorly crystalline and fine-grained iron oxides. Spectra consistent with coarse-grained gray hematite also become more common as colors transition to purple and then gray; thus, we hypothesize that the red crystalline and poorly crystalline hematite were deposited first and then dissolved and reprecipitated as clusters of grains and coarser grains in these units. Coarsening of hematite grains has been observed to occur along diagenetic reaction fronts in terrestrial sedimentary sequences (Beitler et al., 2005; Bowen et al., 2007; Eichhubl et al., 2004; Parry et al., 2009) and frequently results in the bright red to dark red/purple to gray color gradients that we also observe on VRR (Eichhubl et al., 2004). This coarsening process is a form of Ostwald ripening, in which larger, more energetically favorable crystals are formed through dissolution and reprecipitation of smaller grains, which for hematite includes both poorly crystalline and fine-grained red crystalline components (Cornell & Schwertmann, 2003; Eichhubl et al., 2004). In this model, gray Jura bedrock represents the most altered end-member, having undergone local dissolution/reprecipitation or recrystallization of nearly all finer grains. This removal of color, irrespective of process, is typically referred to as bleaching. The retention of coarse-grained gray hematite in gray Jura bedrock after bleaching is also observed in some bleached sedimentary units on Earth (Parry et al., 2009).

This bleaching/coarsening model is supported by the distribution of dark and Fe rich, likely hematite, diagenetic features within bedrock and within sulfate veins on VRR (Bennett et al., 2020; David et al., 2020;

L'Haridon et al., 2020; Tinker et al., 2019). Similar diagenetic features are common in bleached sedimentary units on Earth and form through the same dissolution/reprecipitation process as grain-size coarsening (e.g., Chan & Parry, 2000). Dark diagenetic features are abundant within gray Jura bedrock but less common in red Jura bedrock and the Pettegrove Point member (Bennett et al., 2020; Tinker et al., 2019), suggesting that hematite dissolution and reprecipitation was concentrated in gray Jura bedrock.

We hypothesize that bleaching occurred due to late diagenetic alteration. Given that the dark diagenetic features occur in both the bedrock and within the sulfate veins of the Jura member, at least one bleaching event occurred contemporaneously with vein fill, consistent with a late diagenetic process. Hydrofracturing to produce bedrock fractures requires fluids under high pressure, and bedrock fractures in the Murray formation are hypothesized to have formed either due to burial at depth or sealing by rigid capping units like the Stimson formation (Kronyak et al., 2019). Thus, the gray patches may have formed either at depth or during/after later exhumation. Because bleaching often increases pore space (e.g., Beitler et al., 2005), this may have made gray Jura bedrock susceptible to later secondary reddening. The lack of evidence for secondary reddening in gray Jura bedrock suggests that oxidation of all units to form red crystalline and nanophase hematite likely occurred first and that no widespread oxidation occurred after the late bleaching event. However, small red patches in the Jura member, perhaps including RH, could represent localized secondary reddening or alternatively could be a remnant of earlier processes and indicate an area that experienced a lesser degree of diagenesis.

Local variations in permeability and porosity are the main drivers for patterns of diagenesis in terrestrial sedimentary deposits. The properties of the Jura member suggest more extensive late diagenesis than the Pettegrove Point and Blunts Point members, which must be due to structural impediments or a difference in permeability, pathways, or porosity. Gray Jura bedrock does exhibit a slightly coarser grain size than the Pettegrove Point member based on analysis of the chemical variability between ChemCam spots (Bennett et al., 2020), possibly representing a higher permeability compared to other units. This permeability could be the cause of more intense diagenesis or, alternatively, caused by dissolution during diagenesis. In addition, the Flodigarry facies at the base of the Jura member exhibits complex structural properties (Edgar et al., 2020), which could cause restrictions in fluid flow. The Jura member on VRR may also have been buttressed by more clay-rich Jura bedrock observed in Glen Torridon (Fox et al., 2019; Milliken et al., 2010) or by cemented sandstones of the Stimson formation in the nearby Greenhugh Pediment (Rampe et al., 2020). This could have created a relatively impermeable seal over or around the Jura member on VRR, possibly leading to stagnation of diagenetic fluids within the Jura on VRR and thus more extensive alteration.

Diagenesis may also have affected the strength or hardness of VRR rocks, as defined by drill percussion energy (Fraeman, Edgar, et al., 2020; Jacob et al., 2020). DU and RH required lower percussive energies for the drill to make sufficient rates of progress during drilling, whereas ST and HF both required the maximum percussive energy allowed to make sufficient forward progress during drilling. Voyageurs, Ailsa Craig, Lake Orcadie, and Inverness drill targets were all too hard to successfully drill and thus are likely stronger than HF. Diagenetic cements have the potential to significantly increase the strength of bedrock, especially in the case of sandstones, due to their higher permeability compared to mudstones (e.g., Cook et al., 2014; Marshall & Roering, 2014). Across the Murray formation, rock strength does not exhibit a clear correlation with mineralogy or chemical compositions, but cementing agents that could affect strength may include hematite, Ca sulfate, and/or phyllosilicates (Peters et al., 2018). On VRR, the diversity of diagenetic events may have affected the strength of the rocks in other ways. For example, amorphous silica deposited during diagenesis of the gray Jura (Smith et al., 2020) may also have contributed to strength. Both HF and ST exhibit enhanced silica in their amorphous components compared to other Murray rocks (Rampe et al., 2020), and gray Jura targets generally exhibit enhanced Al_2O_3 and SiO_2 abundance in APXS data compared to other Murray targets (Thompson et al., 2020). Our spectral results also suggest that red crystalline hematite cements are likely prevalent in Pettegrove Point targets Voyageurs and Ailsa Craig based on their color change on drilling and their strong hematite bands. As these targets were too hard to drill, it is possible that hematite cement recrystallized during diagenesis could be contributing to their strength. Sulfate, silica, and hematite cements could all be contributing to the resistant nature of VRR.

Bleaching, hematite grain-size coarsening, and hematite diagenetic feature formation all require that iron was at least locally mobile during diagenesis. ChemCam data show that iron is indeed depleted in bright

zones immediately surrounding dark diagenetic features in gray Jura bedrock, so these "halos" specifically support local iron mobility to form the dark diagenetic features (L'Haridon et al., 2020). These processes, even including large-scale bleaching, do not necessarily require iron mobility at larger scales or significant bulk loss of iron (Parry et al., 2009). Gray Jura bedrock does exhibit slightly lower iron concentrations in APXS bulk chemistry measurements compared to the Pettegrove Point member (Thompson et al., 2020), which could be consistent with some limited larger-scale iron mobility during bleaching. ChemCam chemistry data do not show significant differences in iron abundance between bulk gray Jura bedrock and elsewhere on VRR but do show strong depletions in iron abundance locally, especially around the small-scale halos that are not included in the bulk Jura member observations (David et al., 2020; Frydenvang et al., 2020; L'Haridon et al., 2020). The difference between the datasets could be related to the scale of the measurements, as APXS could be averaging significant small-scale variability like the halos, and thus, the APXS bulk chemistry would include multiple bedrock chemistries that are distinguished at ChemCam scale. Given the high areal abundance of dark diagenetic features in gray Jura bedrock (Bennett et al., 2020; Tinker et al., 2019), the halos themselves could be the main cause of iron loss observed by APXS.

Mobilization of ferric iron like in hematite can occur if fluids become more acidic or reducing (Cornell & Schwertmann, 2003) and in either case is enhanced by the elevated temperatures expected during burial diagenesis at shallow to moderate depths/temperatures reasonable for Gale crater. Reasonable temperatures could range from 30–100°C, as modeled in Borlina et al. (2015) for Hesperian thermal gradient and plausible surface conditions, but are likely limited by observations of hydrated Ca sulfates like bassanite in Murray formation veins that are only stable below ~60°C (Rapin et al., 2016). On Earth, bleaching commonly occurs due to fluids carrying dissolved organic acids, methane, or hydrogen sulfides (Chan & Parry, 2000). While the HF gray Jura sample does not include any detectable clearly acidic minerals like jarosite (Rampe et al., 2020), gray Jura bedrock does show evidence for Al/Si mobility that could be consistent with acidic fluids (Thompson et al., 2020). While an abiotic mechanism for producing reducing hydrocarbon-bearing fluids on Mars is not clear, possible sources may include subsurface sources of methane like magmatic gases or serpentinization. The detection of reduced sulfur in Jura member drill samples by the SAM instrument may support at least somewhat reducing conditions during diagenesis (McAdam et al., 2020; Wong et al., 2020). In addition, the halos are depleted in Mn as well as Fe, which is more consistent with redox-driven processes than acidic fluids (L'Haridon et al., 2020).

6.4. Implications

Gale crater's sedimentary record preserves a complex history of deposition, alteration, and erosion extending across billions of years. Disentangling how habitability varied over time requires a detailed understanding of this complex history. While the lacustrine sediments of the Murray formation provide ample evidence for a long-lived habitable surface environment that could have supported a biosphere in the early Hesperian (Grotzinger et al., 2015), the fate of this biosphere after the lake(s) dried up is unclear. Subsurface fluids on Mars could have supported a subsurface hydrosphere that acted as refugia for surface life during dry periods in Mars history (e.g., Michalski et al., 2013). However, the timing and extent of subsurface processes on Mars and the chemistry of subsurface fluids are poorly constrained.

Our results demonstrate that Gale crater sediments experienced complex postdepositional aqueous interactions over extended periods of time, suggesting a long-lived Martian surface and/or subsurface hydrosphere in this region. The longevity of subsurface fluids is supported by K-Ar ages for diagenetic jarosite in a Murray mudstone sample of 2.12 $\pm$ 0.36 Gyr (Martin et al., 2017). The Murray formation was deposited prior to surface units with crater retention ages ~3.3 to 3.2 Gyr (Grant et al., 2014). Thus, these observations together with our results showing repeated interactions with diagenetic fluids in VRR sediment suggest that groundwater was present in Mt. Sharp, at least intermittently, for more than one half of Mars' history.

The diagenetic processes and associated fluid chemistries that we postulate occurred in VRR sediments are distinct from those identified at previous rover landing sites. Orbital and in situ detections of hematite to date are relatively rare on Mars—in addition to orbital detections in Gale crater (Fraeman et al., 2013), both red and gray hematite detections are primarily limited to Hesperian sediments in Valles Marineris and Meridiani Planum (Arvidson et al., 2006; Bibring et al., 2007; Catling & Moore, 2003; Christensen et al., 2000; Noe Dobrea et al., 2008). However, at these sites, hematite is consistently associated with high abundances of sulfates interpreted to reflect acidic conditions related to photolytic or atmospheric iron oxidation

(Hurowitz & McLennan, 2007). In the Murray formation, hematite is associated with phyllosilicate-bearing mudstones as opposed to sulfates, perhaps reflecting less acidic fluids (Rampe et al., 2017), a more persistent surface environment (Hurowitz et al., 2017), or a different source of oxidation. In addition, widespread bleaching of bedrock by warm and reducing and/or mildly acidic fluids has not been observed at other landing sites, and only one occurrence of possible bleaching has been identified from orbit within light-toned anastomosing structures in Meridiani Planum, hypothesized to be deformation bands (Okubo et al., 2009). This type of diagenetic alteration may have occurred elsewhere on Mars but may be difficult to identify from orbit without detailed analysis of high-resolution color images. Alternatively, the bleaching may be related to conditions relatively unique to Gale crater, perhaps including burial and exhumation in a deep sedimentary basin or a local source for reducing fluids.

The diagenetic processes observed in VRR sediments have major implications for organic and biosignature preservation, as compaction and multiple fluid interactions with changing chemistries, leading to recrystallization and other diagenetic alteration on VRR, are likely to break down organics and could modify other types of biosignatures (Hays et al., 2017). Previous results from MSL have already demonstrated significant local heterogeneity in organic concentrations in Murray mudstones (Freissinet et al., 2015), which may be attributed to diagenesis. However, MSL results also demonstrated that sulfurization during early diagenesis in the hematite-rich Pahrump Hills outcrop in Gale helped to preserve organics (Eigenbrode et al., 2018). Thus, understanding the range of diagenetic processes that occurred on Mars and their spectral and visible signatures in Martian sediments will help MSL and future missions to target biosignature investigations in areas with higher preservation potential.

7. Conclusions

VRR in Gale crater on Mars shows clear evidence for past interactions with diagenetic fluids, which left behind stark color differences between bright red bedrock and dark to light gray bedrock across the ridge, as well as more subtle changes in the red to purple colors of both the Pettegrove Point and Jura members. Based on analysis of Mastcam and ChemCam VNIR spectra, we hypothesize that these variations reflect a complex diagenetic history involving multiple episodes of both early and late fluid flow, which resulted in spatial variations in the crystallinity, grain size, and texture of hematite across the ridge. We hypothesize that oxidation to produce red and nanophase hematite was primarily the result of an early diagenetic process involving meteoric or lacustrine fluids. The last major event was most likely the "bleaching" event that produced the large gray patches, which required significantly different fluid chemistries from those that produced the oxidized "red beds" elsewhere in the Murray and on VRR. This later fluid may have been acidic, reducing, and/or slightly higher temperature. Based on the observed relationships between the gray patches, diagenetic features, and hydrofracturing, we hypothesize that bleaching occurred either at some depth during or after burial, or perhaps during or after later exhumation of VRR. Some localized later secondary oxidation, perhaps during or after exhumation, may have helped produce the variable red colors and red hematite signatures in the Jura and Pettegrove Point members. These results demonstrate that Gale sediments experienced complex postdepositional aqueous interactions over extended periods of time, perhaps on timescales of billions of years. These fluids may have been part of a subsurface hydrosphere that could have supported subsurface habitable environments, but the bleaching and recrystallization process also likely negatively affected biosignature preservation in Gale crater sediments.

Data Availability Statement

All of the Mastcam images used in this manuscript are freely available through the Planetary Data System Cartography and Imaging Sciences node (https://pds-imaging.jpl.nasa.gov/volumes/msl.html), as are all HiRISE images used in this manuscript (https://pds-imaging.jpl.nasa.gov/volumes/mro.html). All of the ChemCam spectra used in this manuscript are freely available through the Planetary Data System Geosciences node (https://pds-geosciences.wustl.edu/missions/msl/chemcam.htm). All Mastcam and ChemCam spectra shown in the manuscript and all calculated spectral parameters are available on Mendeley (https://doi.org/10.17632/w367ty5dr8.1).

Acknowledgments

We thank the MSL mission team for persevering through the challenges of exploration and collecting the data that enabled this work. We also thank Javier Cuadros, Ken Herkenhoff, and an anonymous reviewer for reviews that substantially improved the clarity of the manuscript and Sally Potter-McIntyre and Ken Ridgway for useful discussions regarding diagenesis. Funding for this study was provided by the National Aeronautics and Space Administration (NASA) Mars Science Laboratory Participating Scientist program and the MSL mission. A portion of this research was carried out at the Jet Propulsion Laboratory, California Institute of Technology, under a contract with the NASA. J. F. acknowledges the Carlsberg Foundation (Carlsbergfondet).

References

Adams, J. B. (1968). Lunar and Martian surfaces: Petrologic significance of absorption bands in the near-infrared. *Science*, *159*(3822), 1453–1455. https://doi.org/10.1126/science.159.3822.1453

Anderson, R., & Bell, J. (2010). Geologic mapping and characterization of Gale crater and implications for its potential as a Mars Science Laboratory landing site. *Mars*, *5*, 76–128. https://doi.org/10.1555/mars.2010.0004

Arvidson, R. E., Poulet, F., Morris, R. V., Bibring, J.-P., Bell, J. F. III, Squyres, S. W., et al. (2006). Nature and origin of the hematite-bearing plains of Terra Meridiani based on analyses of orbital and Mars Exploration rover data sets. *Journal of Geophysical Research*, *111*, E12S08. https://doi.org/10.1029/2006JE002728

Beitler, B., Parry, W. T., & Chan, M. A. (2005). Fingerprints of fluid flow: Chemical diagenetic history of the Jurassic Navajo Sandstone, southern Utah, U.S.A. *Journal of Sedimentary Research*, *75*(4), 547–561. https://doi.org/10.2110/jsr.2005.045

Bell, J. F. III, Godber, A., McNair, S., Caplinger, M. A., Maki, J. N., Lemmon, M. T., et al. (2017). The Mars Science Laboratory Curiosity rover Mastcam instruments: Preflight and in-flight calibration, validation, and data archiving. *Earth and Space Science*, *4*, 396–452. https://doi.org/10.1002/2016EA000219

Bennett, K. A., Rivera-Hernandez, F., Tinker, C., Horgan, B., Fey, D. M., Edwards, C., et al. (2020). Extensive diagenesis revealed by fine-scale features at Vera Rubin ridge, Gale crater, Mars. *Journal of Geophysical Research: Planets*. in revision

Bibring, J.-P., Arvidson, R. E., Gendrin, A., Gondet, B., Langevin, Y., Le Mouelic, S., et al. (2007). Coupled ferric oxides and sulfates on the martian surface. *Science*, *317*(5842), 1206–1210. https://doi.org/10.1126/science.1144174

Blake, D., Vaniman, D., Achilles, C., Anderson, R., Bish, D., Bristow, T., et al. (2012). Characterization and calibration of the CheMin mineralogical instrument on Mars Science Laboratory. *Space Science Reviews*, *170*(1-4), 341–399. https://doi.org/10.1007/s11214-012-9905-1

Borlina, C. S., Ehlmann, B. L., & Kite, E. S. (2015). Modeling the thermal and physical evolution of Mount Sharp's sedimentary rocks, Gale crater, Mars: Implications for diagenesis on the MSL Curiosity rover traverse. *Journal of Geophysical Research Planets*, *120*, 1396–1414. https://doi.org/10.1002/2015JE004799

Bowen, B. B., Martini, B. A., Chan, M. A., & Parry, W. T. (2007). Reflectance spectroscopic mapping of diagenetic heterogeneities and fluid-flow pathways in the Jurassic Navajo Sandstone. *AAPG Bulletin*, *91*(2), 173–190. https://doi.org/10.1306/08220605175

Bristow, T. F., Rampe, E. B., Achilles, C. N., Blake, D. F., Chipera, S. J., Craig, P., et al. (2018). Clay mineral diversity and abundance in sedimentary rocks of Gale crater, Mars. *Science Advances*, *4*(6), eaar3330. https://doi.org/10.1126/sciadv.aar3330

Caswell, T. E., & Milliken, R. E. (2017). Evidence for hydraulic fracturing at Gale crater, Mars: Implications for burial depth of the Yellowknife Bay formation. *Earth and Planetary Science Letters*, *468*, 72–84. https://doi.org/10.1016/j.epsl.2017.03.033

Catling, D. C., & Moore, J. M. (2003). The nature of coarse-grained crystalline hematite and its implications for the early environment of Mars. *Icarus*, *165*(2), 277–300. https://doi.org/10.1016/s0019-1035(03)00173-8

Chan, M. A., Bowen, B. B., Parry, W., Ormö, J., & Komatsu, G. (2005). Red rock and red planet diagenesis: Comparisons of Earth and Mars concretions. *GSA Today*, *15*(8), 4. https://doi.org/10.1130/1052-5173(2005)015[4:RRARPD]2.0.CO;2

Chan, M. A., & Parry, W. T. (2000). Diagenetic hematite and manganese oxides and fault-related fluid flow in Jurassic sandstones, southeastern Utah. *AAPG Bulletin*, *84*, 1281–1310. https://doi.org/10.1306/a9673e82-1738-11d7-8645000102c1865d

Christensen, P. R., Bandfield, J. L., Clark, R. N., Edgett, K. S., Hamilton, V. E., Hoefen, T., et al. (2000). Detection of crystalline hematite mineralization on Mars by the Thermal Emission Spectrometer: Evidence for near-surface water. *Journal of Geophysical Research*, *105*(E4), 9623–9642. https://doi.org/10.1029/1999JE001093

Clark, R. N., & Roush, T. L. (1984). Reflectance spectroscopy: Quantitative analysis techniques for remote sensing applications. *Journal of Geophysical Research*, *89*(B7), 6329–6340. https://doi.org/10.1029/JB089iB07p06329

Clark, R. N., Swayze, G. A., Wise, R. A., Livo, K. E., Hoefen, T. M., Kokaly, R. F., & Sutley, S. J. (2007). USGS digital spectral library splib06a (no. 231). US Geological Survey.

Cloutis, E. A., & Gaffey, M. J. (1991). Spectral-compositional variations in the constituent minerals of mafic and ultramafic assemblages and remote sensing implications. *Earth, Moon, and Planets*, *53*(1), 11–53. https://doi.org/10.1007/BF00116217

Cook, J. E., Goodwin, L. B., Boutt, D. F., & Tobin, H. J. (2014). The effect of systematic diagenetic changes on the mechanical behavior of a quartz-cemented sandstone. *Geophysics*, *80*(2), D145–D160. https://doi.org/10.1190/GEO2014-0026.1

Cornell, R. M., & Schwertmann, U. (2003). *The iron oxides: Structure, properties, reactions, occurrences and uses*. Weinheim, Germany: Wiley-VCH. https://doi.org/10.1002/3527602097

Crisp, J. A., Adler, M., Matijevic, J. R., Squyres, S. W., Arvidson, R. E., & Kass, D. M. (2003). Mars Exploration Rover mission. *Journal of Geophysical Research*, *108*(E12), 8061. https://doi.org/10.1029/2002JE002038

David, G., Cousin, A., Forni, O., Meslin, P. Y., Dehouck, E., Mangold, N., et al. (2020). Analyses of high-iron sedimentary bedrock and diagenetic features observed with ChemCam at Vera Rubin ridge, Gale crater, Mars: Calibration and characterization. *Journal of Geophysical Research: Planets*. https://doi.org/10.1029/2019JE006314

Edgar, L. A., Fedo, C. M., Gupta, S., Banham, S. G., Fraeman, A. A., Grotzinger, J. P., et al. (2020). A lacustrine paleoenvironment recorded at Vera Rubin ridge, Gale crater: Overview of the sedimentology and stratigraphy observed by the Mars Science Laboratory Curiosity rover. *Journal of Geophysical Research: Planets*, *125*. https://doi.org/10.1029/2019JE006307

Edgett, K. S. (2016). *The other sedimentary rocks of early Mars*. Paper presented at 47th Lunar and Planetary Science Conference, abstract #1379.

Eichhubl, P., Taylor, W. L., Pollard, D. D., & Aydin, A. (2004). Paleo-fluid flow and deformation in the Aztec Sandstone at the Valley of Fire, Nevada—Evidence for the coupling of hydrogeologic, diagenetic, and tectonic processes. *Geological Society of America Bulletin*, *116*(9), 1120–1117. https://doi.org/10.1130/B25446.1

Eigenbrode, J. L., Summons, R. E., Steele, A., Freissinet, C., Millan, M., Navarro-González, R., et al. (2018). Organic matter preserved in 3-billion-year-old mudstones at Gale crater, Mars. *Science*, *360*(6393), 1096–1101. https://doi.org/10.1126/science.aas9185

Fedo, C. M., Grotzinger, J. P., Gupta, S., Banham, S., Bennett, K., Edgar, L., et al. (2019). Evidence for persistent, water-rich, lacustrine deposition preserved in the Murray formation, Gale crater: A depositional system suitable for sustained habitability. *Ninth International Conference on Mars*, *#6308*.

Fedo, C. M., Grotzinger, J. P., Gupta, S., Fraeman, A., Edgar, L., Edgett, K., et al. (2018). *Sedimentology and stratigraphy of the Murray formation, Gale crater, Mars*. 49th Lunar and Planetary Science Conference, #2078.

Fox, V. K., Bennett, K. A., Bristow, T., Ehlmann, B., House, C., Fairén, A. G., et al. (2019). Exploring the clay-bearing unit with the Curiosity rover, *50th Lunar and Planetary Science Conference*, #2826.

Fraeman, A. A., Arvidson, R. E., Catalano, J. G., Grotzinger, J. P., Morris, R. V., Murchie, S. L., et al. (2013). A hematite-bearing layer in Gale crater, Mars: Mapping and implications for past aqueous conditions. *Geology*, *41*(10), 1103–1106. https://doi.org/10.1130/G34613.1

Fraeman, A. A., Edgar, L. A., Rampe, E. B., Thompson, L. M., Frydenvang, J., Fedo, C. M., et al. (2020). Evidence for a diagenetic origin of Vera Rubin ridge, Gale crater, Mars: Summary and synthesis of Curiosity's exploration campaign. *Journal of Geophysical Research: Planets*. https://doi.org/10.1029/2020JE006527

Fraeman, A. A., Ehlmann, B. L., Arvidson, R. E., Edwards, C. S., Grotzinger, J. P., Milliken, R. E., et al. (2016). The stratigraphy and evolution of lower Mount Sharp from spectral, morphological, and thermophysical orbital data sets. *Journal of Geophysical Research: Planets*, *121*, 1713–1736. https://doi.org/10.1002/2016JE005095

Fraeman, A. A., Johnson, J. R., Arvidson, R. E., Rice, M. S., Wellington, D. F., Morris, R. V., et al. (2020). Synergistic ground and orbital observations of iron oxides on Mt. Sharp and Vera Rubin ridge. *Journal of Geophysical Research: Planets*, *125*. https://doi.org/10.1029/2019JE006294

Freissinet, C., Glavin, D. P., Mahaffy, P. R., Miller, K. E., Eigenbrode, J. L., Summons, R. E., et al. (2015). Organic molecules in the Sheepbed Mudstone, Gale Crater, Mars. *Journal of Geophysical Research: Planets*, *120*, 495–514. https://doi.org/10.1002/2014JE004737

Frydenvang, J., Gasda, P. J., Hurowitz, J. A., Grotzinger, J. P., Wiens, R. C., Newsom, H. E., et al. (2017). Diagenetic silica enrichment and late-stage groundwater activity in Gale crater, Mars. *Geophysical Research Letters*, *44*, 4716–4724. https://doi.org/10.1002/2017GL073323

Frydenvang, J., Mangold, N., Wiens, R. C., Fraeman, A. A., Edgar, L. A., Fedo, C. M., et al. (2020). The chemostratigraphy of the Murray formation and role of diagenesis at Vera Rubin ridge in Gale crater, Mars, as observed by the ChemCam instrument. *Journal of Geophysical Research: Planets*, *125*. https://doi.org/10.1029/2019JE006320

Gillespie, A., Kahle, A., & Walker, R. (1986). Color enhancement of highly correlated images. I. Decorrelation and HSI contrast stretches. *Remote Sensing of Environment*, *20*(3), 209–235. https://doi.org/10.1016/0034-4257(86)90044-1

Grant, J. A., Wilson, S. A., Mangold, N., Calef, F., & Grotzinger, J. P. (2014). The timing of alluvial activity in Gale crater. *Mars*, *41*(4), 1142–1149. https://doi.org/10.1002/2013GL058909

Grotzinger, J., Beaty, D., Dromart, G., Gupta, S., Harris, M., Hurowitz, J., et al. (2011). Mars sedimentary geology: Key concepts and outstanding questions. *Astrobiology*, *11*(1), 77–87. https://doi.org/10.1089/ast.2010.0571

Grotzinger, J. P., Arvidson, R. E., Bell, J. F. III, Calvin, W., Clark, B. C., Fike, D. A., et al. (2005). Stratigraphy and sedimentology of a dry to wet eolian depositional system, Burns formation, Meridiani Planum, Mars. *Earth and Planetary Science Letters*, *240*(1), 11–72. https://doi.org/10.1016/j.epsl.2005.09.039

Grotzinger, J. P., Crisp, J., Vasavada, A. R., Anderson, R. C., Baker, C. J., Barry, R., et al. (2012). Mars Science Laboratory mission and science investigation. *Space Science Reviews*, *170*(1–4), 5–56. https://doi.org/10.1007/s11214-012-9892-2

Grotzinger, J. P., Gupta, S., Malin, M. C., Rubin, D. M., Schieber, J., Siebach, K., et al. (2015). Deposition, exhumation, and paleoclimate of an ancient lake deposit, Gale crater, Mars. *Science*, *350*(6257), aac7575. https://doi.org/10.1126/science.aac7575

Grotzinger, J. P., & Milliken, R. (2012). The sedimentary rock record of Mars: Distribution, origins, and global stratigraphy. In *Sedimentary geology of Mars*, *SEPM Special Publication* (Vol. 102, pp. 1–48). Tulsa, Oklahoma: SEPM (Society for Sedimentary Geology).

Grotzinger, J. P., Sumner, D. Y., Kah, L. C., Stack, K., Gupta, S., Edgar, L., et al. (2014). A habitable fluvio-lacustrine environment at Yellowknife Bay, Gale crater, Mars. *Science*, *343*(6169), 1242777–1,242,777. https://doi.org/10.1126/science.1242777

Guzewich, S. D., Lemmon, M., Smith, C. L., Martínez, G., Vicente-Retortillo, Á., Newman, C. E., et al. (2019). Mars Science Laboratory observations of the 2018/Mars year 34 global dust storm. *Geophysical Research Letters*, *46*, 71–79. https://doi.org/10.1029/2018GL080839

Hays, L. E., Graham, H. V., Des Marais, D. J., Hausrath, E. M., Horgan, B., McCollom, T. M., et al. (2017). Biosignature preservation and detection in Mars analog environments. *Astrobiology*, *17*(4), 363–400. https://doi.org/10.1089/ast.2016.1627

Horgan, B. H. N., Cloutis, E. A., Mann, P., & Bell, J. F. (2014). Near-infrared spectra of ferrous mineral mixtures and methods for their identification in planetary surface spectra. *Icarus*, *234*, 132–154. https://doi.org/10.1016/j.icarus.2014.02.031

Hurowitz, J. A., Grotzinger, J. P., Fischer, W. W., McLennan, S. M., Milliken, R. E., Stein, N., et al. (2017). Redox stratification of an ancient lake in Gale crater, Mars. *Science*, *356*(6), eaah6849. https://doi.org/10.1126/science.aah6849

Hurowitz, J. A., & McLennan, S. M. (2007). A ~3.5 Ga record of water-limited, acidic weathering conditions on Mars. *Earth and Planetary Science Letters*, *260*(3–4), 432–443. https://doi.org/10.1016/j.epsl.2007.05.043

Jacob, S. R., Wellington, D. F., Bell, J. F. III, Achilles, C., Fraeman, A. A., Horgan, B., et al. (2020). Spectral, compositional, and physical properties of the upper Murray formation and Vera Rubin ridge, Gale crater, Mars. *Journal of Geophysical Research: Planets*. https://doi.org/10.1029/2019JE006290

Johnson, A. H. (1976). Palaeomagnetism of the Jurassic Navajo Sandstone from south-western Utah. *Geophysical Journal*, *44*(1), 161–175. https://doi.org/10.1111/j.1365-246X.1976.tb00280.x

Johnson, J. R., Achilles, C., Bell, J. F. III, Bender, S., Cloutis, E., Ehlmann, B., et al. (2017). Visible/near-infrared spectral diversity from in situ observations of the Bagnold Dune Field sands in Gale Crater, Mars. *Journal of Geophysical Research: Planets*, *122*, 2655–2684. https://doi.org/10.1002/2016JE005187

Johnson, J. R., Bell, J. F. III, Bender, S., Blaney, D., Cloutis, E., DeFlores, L., et al. (2015). ChemCam passive reflectance spectroscopy of surface materials at the Curiosity landing site, Mars. *Icarus*, *249*, 74–92. https://doi.org/10.1016/j.icarus.2014.02.028

Johnson, J. R., Bell, J. F. III, Bender, S., Blaney, D., Cloutis, E., Ehlmann, B., et al. (2016). Constraints on iron sulfate and iron oxide mineralogy from ChemCam visible/near-infrared reflectance spectroscopy of Mt. Sharp basal units, Gale Crater, Mars. *American Mineralogist*, *101*(7), 1501–1514. https://doi.org/10.2138/am-2016-5553

Johnson, S. A., Glover, B. W., & Turner, P. (1997). Multiphase reddening and weathering events in Upper Carboniferous red beds from the English West Midlands. *Journal of the Geological Society*, *154*(4), 735–745. https://doi.org/10.1144/gsjgs.154.4.0735

Kinch, K. M., Bell, J. F. I., Goetz, W., Johnson, J. R., Joseph, J., Madsen, M. B., & Sohl-Dickstein, J. (2015). Dust deposition on the decks of the Mars Exploration Rovers: 10 years of dust dynamics on the Panoramic Camera calibration targets. *Earth and Space Science*, *2*(5), 144–172. https://doi.org/10.1002/2014EA000073

Kronyak, R. E., Kah, L. C., Edgett, K. S., VanBommel, S. J., Thompson, L. M., Wiens, R. C., et al. (2019). Mineral-filled fractures as indicators of multigenerational fluid flow in the Pahrump Hills member of the Murray formation, Gale crater, Mars. *Earth and Space Science*, *6*, 238–265. https://doi.org/10.1029/2018EA000482

L'Haridon, J., Mangold, N., Fraeman, A. A., Johnson, J. R., Cousin, A., Rapin, W., et al. (2020). Iron mobility during diagenesis at Vera Rubin ridge, Gale crater, Mars. *Journal of Geophysical Research: Planets*. https://doi.org/10.1029/2019JE006299

L'Haridon, J., Mangold, N., Meslin, P.-Y. Y., Johnson, J. R., Rapin, W., Forni, O., et al. (2018). Chemical variability in mineralized veins observed by ChemCam on the lower slopes of Mount Sharp in Gale crater, Mars. *Icarus*, *311*, 69–86. https://doi.org/10.1016/j.icarus.2018.01.028

Lane, M. D., Morris, R. V., Mertzman, S. A., & Christensen, P. R. (2002). Evidence for platy hematite grains in Sinus Meridiani, Mars. *Journal of Geophysical Research*, *107*(E12), 5126. https://doi.org/10.1029/2001JE001832

Lemmon, M. T., Guzewich, S. D., McConnochie, T., Vicente Retortillo, Á., Martínez, G., Smith, M. D., et al. (2019). Large dust aerosol sizes seen during the 2018 Martian global dust event by the Curiosity rover. *Geophysical Research Letters*, *46*, 9448–9456. https://doi.org/10.1029/2019GL084407

Malin, M. C., & Edgett, K. S. (2000). Sedimentary rocks of early Mars. *Science*, *290*(5498), 1927–1937. https://doi.org/10.1126/science.290.5498.1927

Malin, M. C., & Edgett, K. S. (2001). Mars global surveyor Mars orbiter camera: Interplanetary cruise through primary mission. *Journal of Geophysical Research*, *106*(E10), 23,429–23,570. https://doi.org/10.1029/2000JE001455

Malin, M. C., Ravine, M. A., Caplinger, M. A., Tony Ghaemi, F., Schaffner, J. A., Maki, J. N., et al. (2017). The Mars Science Laboratory (MSL) Mast cameras and Descent imager: Investigation and instrument descriptions. *Earth and Space Science*, *4*, 506–539. https://doi.org/10.1002/2016EA000252

Marshall, J. A., & Roering, J. J. (2014). Diagenetic variation in the Oregon Coast Range: Implications for rock strength, soil production, hillslope form, and landscape evolution. *Journal of Geophysical Research: Earth Surface*, *119*, 1395–1417. https://doi.org/10.1002/2013JF003004

Martin, P. E., Farley, K. A., Baker, M. B., Malespin, C. A., Schwenzer, S. P., Cohen, B. A., et al. (2017). A two-step K-Ar experiment on Mars: Dating the diagenetic formation of Jarosite from Amazonian groundwaters. *Journal of Geophysical Research: Planets*, *122*, 2803–2818. https://doi.org/10.1002/2017JE005445

Maurice, S., Wiens, R. C., Saccoccio, M., Barraclough, B., Gasnault, O., Forni, O., et al. (2012). The ChemCam instrument suite on the Mars Science Laboratory (MSL) rover: Science objectives and mast unit description. *Space Science Reviews*, *170*(1–4), 95–166. https://doi.org/10.1007/s11214-012-9912-2

McAdam, A. C., Sutter, B., Archer, P. D., Franz, H. B., Wong, G. M., Lewis, J. M. T., et al. (2020). Constraints on the mineralogy and geochemistry of the Vera Rubin ridge, Gale crater, Mars, from Mars Science Laboratory sample analysis at Mars evolved gas analyses. *Journal of Geophysical Research: Planets*. https://doi.org/10.1029/2019JE006309

Mcewen, A. S., Eliason, E. M., Bergstrom, J. W., Bridges, N. T., Hansen, C. J., Delamere, W. A., et al. (2007). Mars reconnaissance orbiter's High Resolution Imaging Science Experiment (HiRISE). *Journal of Geophysical Research*, *112*, E05S02. https://doi.org/10.1029/2005JE002605

Mclennan, S. M., Bell, J. F. III, Calvin, W. M., Christensen, P. R., Clark, B. C., de Souza, P. A., et al. (2005). Provenance and diagenesis of the evaporite-bearing Burns formation, Meridiani Planum, Mars. *Earth and Planetary Science Letters*, *240*(1), 95–121. https://doi.org/10.1016/j.epsl.2005.09.041

McLennan, S. M., Grotzinger, J. P., Hurowitz, J. A., & Tosca, N. J. (2018). The sedimentary cycle on early Mars. *Annual Review of Earth and Planetary Sciences*, *47*(1), annurev–earth–053018–060332–28. https://doi.org/10.1146/annurev-earth-053018-060332

Metcalfe, R., Rochelle, C. A., Savage, D., & Higgo, J. W. (1994). Fluid-rock interactions during continental red bed diagenesis: Implications for theoretical models of mineralization in sedimentary basins. *Geological Society*, *78*(1), 301–324. https://doi.org/10.1144/GSL.SP.1994.078.01.21

Michalski, J. R., Cuadros, J., Niles, P. B., Parnell, J., Rogers, A. D., & Wright, S. P. (2013). Groundwater activity on Mars and implications for a deep biosphere. *Nature Geoscience*, 1–6. https://doi.org/10.1038/ngeo1706

Milliken, R. E., Ewing, R. C., Fischer, W. W., & Hurowitz, J. (2014). Wind-blown sandstones cemented by sulfate and clay minerals in Gale crater. *Mars*, *41*(4), 1149–1154. https://doi.org/10.1002/2013GL059097

Milliken, R. E., Grotzinger, J. P., & Thomson, B. J. (2010). Paleoclimate of Mars as captured by the stratigraphic record in Gale Crater. *Geophysical Research Letters*, *37*, L04201. https://doi.org/10.1029/2009GL041870

Mitra, K., & Catalano, J. G. (2019). Chlorate as a potential oxidant on Mars: Rates and products of dissolved Fe(II) oxidation. *Journal of Geophysical Research: Planets*, *124*, 2893–2916. https://doi.org/10.1029/2019JE006133

Montañez, I. P., & Crossey, L. J. (2018). Diagenesis. In W. M. White (Ed.), *Encyclopedia of geochemistry* (Vol. 44, pp. 21–23). Cham: Springer International Publishing. https://doi.org/10.1007/978-3-319-39312-4_35

Morris, R. V., Agresti, D. G., Lauer, H. V., Newcomb, J. A., Shelfer, T. D., & Murali, A. V. (1989). Evidence for pigmentary hematite on Mars based on optical, magnetic, and Mossbauer studies of superparamagnetic (nanocrystalline) hematite. *Journal of Geophysical Research*, *94*(B3), 2760–2778. https://doi.org/10.1029/JB094iB03p02760

Morris, R. V., Golden, D. C., Bell, J. F. I., Lauer, H. V. J., & Adams, J. B. (1993). Pigmenting agents in Martian soils—Inferences from spectral, Moessbauer, and magnetic properties of nanophase and other iron oxides in Hawaiian palagonitic soil PN-9. *Geochimica et Cosmochimica Acta*, *57*(19), 4597. https://doi.org/10.1016/0016-7037(93)90185-Y

Morris, R. V., & Lauer, H. V. (1990). Matrix effects for reflectivity spectra of dispersed nanophase (superparamagnetic) hematite with application to Martian spectral data. *Journal of Geophysical Research*, *95*(B4), 5101–5109. https://doi.org/10.1029/JB095iB04p05101

Morris, R. V., Lawson, C. A., Gibson, E. K. J., Lauer, H. V. J., Nace, G. A., & Stewart, C. (1985). Spectral and other physicochemical properties of submicron powders of hematite (α-Fe_2O_3), maghemite (γ-Fe_2O_3), magnetite (Fe_3O_4), goethite (α-FeOOH), and lepidocrocite (γ-FeOOH). *Journal of Geophysical Research*, *90*, 3126–3144. https://doi.org/10.1029/JB090iB04p03126

Morris, R. V., & Neely, S. C. (1982). Optical properties of hematite-magnetite mixtures: Implications for Mars, Lunar and Planetary Science XIII, 548–549.

Mücke, A. (1994). Chapter 11 part I. Postdiagenetic ferruginization of sedimentary rocks (sandstones, oolitic ironstones, kaolins and bauxites)—Including a comparative study of the reddening of red beds. In *Diagenesis, IV. Developments in sedimentology* (Vol. 51, pp. 361–395). Amsterdam, The Netherlands: Elsevier.

Nachon, M., Clegg, S. M., Mangold, N., Schröder, S., Kah, L. C., Dromart, G., et al. (2014). Calcium sulfate veins characterized by ChemCam/Curiosity at Gale crater, Mars. *Journal of Geophysical Research: Planets*, *119*, 1991–2016. https://doi.org/10.1002/2013JE004588

Nachon, M., Mangold, N., Forni, O., Kah, L. C., Cousin, A., Wiens, R. C., et al. (2017). Chemistry of diagenetic features analyzed by ChemCam at Pahrump Hills, Gale crater, Mars. *Icarus*, *281*, 121–136. https://doi.org/10.1016/j.icarus.2016.08.026

Nachon, M., Mangold, N., Forni, O., Kah, L. C., Cousin, A., Wiens, R. C., et al. (2016). Chemistry of diagenetic features analyzed by ChemCam at Pahrump Hills, Gale crater, Mars. *Icarus*, *281*, 121–136. https://doi.org/10.1016/j.icarus.2016.08.026

Noe Dobrea, E. Z., Poulet, F., & Malin, M. C. (2008). Correlations between hematite and sulfates in the chaotic terrain east of Valles Marineris. *Icarus*, *193*(2), 516–534. https://doi.org/10.1016/j.icarus.2007.06.029

Okubo, C. H., Schultz, R. A., Chan, M. A., & Komatsu, G. (2009). Deformation band clusters on Mars and implications for subsurface fluid flow. *Geological Society of America Bulletin*, *121*(3–4), 474–482. https://doi.org/10.1130/B26421.1

Parry, W. T., & Chan, M. A. (2004). Chemical bleaching indicates episodes of fluid flow in deformation bands in sandstone. *AAPG Bulletin*, *88*(2), 175–191. https://doi.org/10.1306/09090303034

Parry, W. T., Chan, M. A., & Nash, B. P. (2009). Diagenetic characteristics of the Jurassic Navajo Sandstone in the Covenant oil field, central Utah thrust belt. *AAPG Bulletin*, *93*(8), 1039–1061. https://doi.org/10.1306/04270908170

Peters, G. H., Carey, E. M., Anderson, R. C., Abbey, W. J., Kinnett, R., Watkins, J. A., et al. (2018). Uniaxial compressive strengths of rocks drilled at Gale Crater, Mars. *Geophysical Research Letters*, *45*, 108–116. https://doi.org/10.1002/2017GL075965

Potter-McIntyre, S. L., Chan, M. A., & McPherson, B. J. (2014). Concretion formation in volcaniclastic host rocks: Evaluating the role of organics, mineralogy, and geochemistry on early diagenesis. *Journal of Sedimentary Research*, *84*(10), 875–892. https://doi.org/10.2110/jsr.2014.58

Rampe, E. B., Bristow, T. F., Morris, R. V., Morrison, S. M., Achilles, C. N., Ming, D. W., et al. (2020). Mineralogy of Vera Rubin ridge from the Mars Science Laboratory CheMin instrument. *Journal of Geophysical Research: Planets*, *125*. https://doi.org/10.1029/2019JE006306

Rampe, E. B., Ming, D. W., Blake, D. F., Bristow, T. F., Chipera, S. J., Grotzinger, J. P., et al. (2017). Mineralogy of an ancient lacustrine mudstone succession from the Murray formation, Gale crater, Mars. *Earth and Planetary Science Letters*, *471*, 172–185. https://doi.org/10.1016/j.epsl.2017.04.021

Rapin, W., Ehlmann, B. L., Dromart, G., Schieber, J., Thomas, N. H., Fischer, W. W., et al. (2019). An interval of high salinity in ancient Gale crater lake on Mars. *Nature Geoscience*, *12*(11), 889–895. https://doi.org/10.1038/s41561-019-0458-8

Rapin, W., Meslin, P.-Y., Maurice, S., Vaniman, D., Nachon, M., Mangold, N., et al. (2016). Hydration state of calcium sulfates in Gale crater, Mars: Identification of bassanite veins. *Earth and Planetary Science Letters*, *452*, 197–205. https://doi.org/10.1016/j.epsl.2016.07.045

Rice, M. S, Bell, J. F., Cloutis, E. A., Wang, A., Ruff, S. W., Craig, M. A., et al. (2010). Silica-rich deposits and hydrated minerals at Gusev Crater, Mars: Vis-NIR spectral characterization and regional mapping. *Icarus*, *205*(2), 375–395. https://doi.org/10.1016/j.icarus.2009.03.035

Rice, M. S., Cloutis, E. A., Bell, J. F., Bish, D. L., Horgan, B. H., Mertzman, S. A., et al. (2013). Reflectance spectra diversity of silica-rich materials: Sensitivity to environment and implications for detections on Mars. *Icarus*, *223*(1), 499–533. https://doi.org/10.1016/j.icarus.2012.09.021

Rivera-Hernández, F., Sumner, D. Y., Mangold, N., Banham, S. G., Edgett, K. S., Fedo, C. M., et al. (2020). Grain size variations in the murray formation: Stratigraphic evidence for changing depositional environments in Gale Crater, Mars. *Journal of Geophysical Research: Planets*, *125*, 279–318. https://doi.org/10.1029/2019JE006230

Ruff, S. W., Farmer, J. D., Calvin, W. M., Herkenhoff, K. E., Johnson, J. R., Morris, R. V., et al. (2011). Characteristics, distribution, origin, and significance of opaline silica observed by the Spirit rover in Gusev crater, Mars. *Journal of Geophysical Research*, *116*, E00F23. https://doi.org/10.1029/2010JE003767

Ruff, S. W., Niles, P. B., Alfano, F., & Clarke, A. B. (2014). Evidence for a Noachian-aged ephemeral lake in Gusev crater, Mars. *Geology*, *42*(4), 359–362. https://doi.org/10.1130/G35508.1

Schwertmann, U. (1993). Relations between iron oxides, soil color, and soil formation. In *Soil color*, *SSSA Special Publication no 31* (pp. 51–69). Madison, Wisconsin: Soil Science Society of America.

Sheldon, N. (2005). Do red beds indicate paleoclimatic conditions?: A Permian case study. *Palaeogeography, Palaeoclimatology, Palaeoecology*, *228*(3–4), 305–319. https://doi.org/10.1016/j.palaeo.2005.06.009

Sherman, D. M. (1990). *Crystal chemistry, electronic structures, and spectra of Fe sites in clay minerals: Applications to photochemistry and electron transport*, *ACS Symposium Series* (Chap 15, pp. 284–309). Washington, DC: American Chemical Society.

Siebach, K. L., Grotzinger, J. P., Kah, L. C., Stack, K. M., Malin, M., Léveillé, R., & Sumner, D. Y. (2014). Subaqueous shrinkage cracks in the Sheepbed mudstone: Implications for early fluid diagenesis, Gale crater, Mars. *Journal of Geophysical Research: Planets*, *119*, 1597–1613. https://doi.org/10.1002/2014JE004623

Smith, C. L., Moores, J. E., Lemmon, M., Guzewich, S. D., Moore, C. A., Ellison, D., & Khayat, A. S. J. (2019). Visibility and line-of-sight extinction estimates in Gale crater during the 2018/MY34 global dust storm. *Geophysical Research Letters*, *46*, 9414–9421. https://doi.org/10.1029/2019GL083788

Smith, R. J., McLennan, S. M., Dehouck, E., Horgan, B., Jacob, S., Mangold, N., et al. (2020). *Exploring silica diagenesis in Gale Crater, Mars using the chemostratigraphy of x-ray amorphous materials*. Paper presented at 51st Lunar & Planetary Science Conference, abstract #2708.

Stack, K. M., Grotzinger, J. P., Kah, L. C., Schmidt, M. E., Mangold, N., Edgett, K. S., et al. (2014). Diagenetic origin of nodules in the Sheepbed member, Yellowknife Bay formation, Gale crater, Mars. *Journal of Geophysical Research: Planets*, *119*, 1637–1664. https://doi.org/10.1002/2014JE004617

Summons, R. E., Amend, J. P., Bish, D., Buick, R., Cody, G. D., Des Marais, D. J., et al. (2011). Preservation of Martian organic and environmental records: Final report of the Mars Biosignature Working Group. *Astrobiology*, *11*(2), 157–181. https://doi.org/10.1089/ast.2010.0506

Sun, V. Z., Stack, K. M., Kah, L. C., Thompson, L., Fischer, W., Williams, A. J., et al. (2018). Late-stage diagenetic concretions in the Murray formation, Gale crater, Mars. *Icarus*, *321*, 866–890. https://doi.org/10.1016/j.icarus.2018.12.030

Thompson, L. M., Berger, J. A., Spray, J. G., Fraeman, A. A., McCraig, M. A., O'Connell-Cooper, C. D., et al. (2020). APXS-derived compositional characteristics of the Vera Rubin ridge, Gale crater, Mars: Geochemical implications for the origin of the ridge. *Journal of Geophysical Research: Planets*. https://doi.org/10.1029/2019JE006319

Thomson, B. J., Bridges, N. T., Milliken, R., Baldridge, A., Hook, S. J., Crowley, J. K., et al. (2011). Constraints on the origin and evolution of the layered mound in Gale crater, Mars using Mars reconnaissance Orbiter data. *Icarus*, *214*(2), 413–432. https://doi.org/10.1016/j.icarus.2011.05.002

Tinker, C. R., Horgan, B., & Bennett, K. (2019). Morphology and occurrence of dark toned diagenetic features in the Vera Rubin ridge, Gale crater, Mars from MAHLI color images, *50th Lunar and Planetary Science Conference*, #1730.

Torrent, J., & Schwertmann, U. (1987). Influence of hematite on the color of red beds. *SEPM Journal of Sedimentary Research*, *57*. https://doi.org/10.1306/212f8bd4-2b24-11d7-8648000102c1865d

Townsend, T. E. (1987). Discrimination of iron alteration minerals in visible and near-infrared reflectance data. *Journal of Geophysical Research*, *92*(B2), 1441. https://doi.org/10.1029/JB092iB02p01441

Van Houten, F. B. (1973). Origin of red beds: A review—1961–1972. *Annual Review of Earth and Planetary Sciences*, *1*(1), 39–61. https://doi.org/10.1146/annurev.ea.01.050173.000351

Walker, T. (1976). Diagenetic origin of continental red beds. In *The continental Permian in central, west, and south Europe* (pp. 240–282). Dordrecht-Holland: D. Reidel Publishing Company.

Walker, T. R., Larson, E. E., & Hoblitt, R. P. (1981). Nature and origin of hematite in the Moenkopi Formation (Triassic), Colorado Plateau: A contribution to the origin of magnetism in red beds. *Journal of Geophysical Research*, *86*(B1), 317–333. https://doi.org/10.1029/JB086iB01p00317

Wellington, D. F., Bell, J. F. I., Johnson, J. R., Kinch, K. M., Rice, M. S., Godber, A., et al. (2017). Visible to near-infrared MSL/Mastcam multispectral imaging: Initial results from select high-interest science targets within Gale Crater, Mars. *American Mineralogist*, *102*(6), 1202–1217. https://doi.org/10.2138/am-2017-5760CCBY

Wiens, R. C., Maurice, S., Barraclough, B., Saccoccio, M., Barkley, W. C., Bell, J. F. III, et al. (2012). The ChemCam instrument suite on the Mars Science Laboratory (MSL) rover: Body unit and combined system tests. *Space Science Reviews*, *170*(1-4), 167–227. https://doi.org/10.1007/s11214-012-9902-4

Wiens, R. C., Maurice, S., Lasue, J., Forni, O., Anderson, R. B., Clegg, S., et al. (2013). Pre-flight calibration and initial data processing for the ChemCam laser-induced breakdown spectroscopy instrument on the Mars Science Laboratory rover. *Spectrochimica Acta Part B: Atomic Spectroscopy*, *82*, 1–27. https://doi.org/10.1016/j.sab.2013.02.003

Wong, G. M., Lewis, J. M. T., Knudson, C. A., Millan, M., McAdam, A. C., Eigenbrode, J. L., et al. (2020). Detection of reduced sulfur on Vera Rubin ridge by quadratic discriminant analysis of volatiles observed during evolved gas analysis. *Journal of Geophysical Research: Planets*, *125*. https://doi.org/10.1029/2019JE006304

Yen, A. S., Ming, D. W., Vaniman, D. T., Gellert, R., Blake, D. F., Morris, R. V., et al. (2017). Multiple stages of aqueous alteration along fractures in mudstone and sandstone strata in Gale Crater, Mars. *Earth and Planetary Science Letters*, *471*, 186–198. https://doi.org/10.1016/j.epsl.2017.04.033